2016

Coupling of Laser Beams for Filament Propagation

Daniel Kepler
University of Central Florida

COUPLING OF LASER BEAMS FOR FILAMENT PROPAGATION

by

DANIEL J. KEPLER
B.S. University of Central Florida, 2014

A thesis submitted in partial fulfillment of the requirements
for the degree of Master of Science
in the College of Optics and Photonics
at the University of Central Florida
Orlando, Florida

Spring Term
2016

Major Professor: Martin C. Richardson

ABSTRACT

Laser filamentation is a nonlinear process involving high-energy, ultrashort pulses that create narrow, non-diffracting structures over many times the Raleigh length. While many of the characteristics of filaments can vary greatly depending on the physical parameters used to create them, they share several defining features: a high intensity core, a lower intensity cladding of photons that serves as an energy reservoir to the core, and spectral broadening into a supercontinuum. While there have been many studies on the creation and control of multiple filaments from one laser pulse and a few studies on the interaction of two single filaments, many fundamental questions concerning the nature of this interaction still exist.

This thesis seeks to explore the correlation between ultrashort pulses involving spatial separation, temporal delay, and relative degree of polarization using an interferometric approach. Evaluating the beam profiles and spectrum that result from varying those parameters.

ACKNOWLEDGMENTS

I would like to acknowledge the support of my advisor, Dr. Martin Richardson, who gave me the opportunity to join LPL (Laser Plasma Laboratory) and first guided me into the extraordinary field of filamentation. I would like to also thank the other members of my committee, Dr Matthieu Baudelet and Dr. Demetrios Christodoulides, for their time and thoughts.

Dr. Michael Chini and Dr. Lawrence Shah have been a great help with their excellent insights and thought experiments. Their perspective and expertise on the problems that arose during research was priceless. Though a recent addition to LPL, Dr. Shermineh Rostami helped to keep me motivated and was instrumental in getting solutions to coding issues and the unexpected phenomena that sometimes arose.

Many of the professors at CREOL (Center for Research and Education in Optics and Lasers) have been essential as instructors, but I'd like to commend Dr. Peter Delfyett and Dr. Pieter Kik, whom each have a special passion and ability to inspire and pass on knowledge. They set the gold standard for what it means to be an instructor.

Khan Lim and CheonHa Jeon were the best peer mentors I could have asked for and their contributions are not only valuable to me, but a true cornerstone to all the research of the filamentation group. They were always willing to take time out their busy schedules to answer my many, many questions.

I would like to thank my good friends, Patrick Roumayah and Ethan ‘Jesse’ Lane. The impromptu hallway meetings we had provided countless “Eureka!” moments for our schoolwork and my research. The levity they added created some of the most spirited highlights of my time at CREOL.

To do any of this research, I needed the appropriate equipment. To that end, a special acknowledgement to Joshua Bradford and Nathan Bodnar; the long hours that they put in to support the MTFL (Multi-Terawatt Femtosecond Laser) were critical to obtaining a large portion of the data in this thesis. Their patience and dedication are second to none. Similarly, I’d like to thank John Szilagyi for teaching me the importance of good plumbing.

It’s impossible to give everyone the proper thanks they deserve, but I’d like to thank all the past and current members of LPL as well as CREOL at large that have made my time here so special with special mentions to Danielle Reyes, Daniel Thul, Haley Kerrigan, Evelyn Strunk, Dr. Ayman Abouraddy, Dr. Aristide Dogariu, Dr. M. G. "Jim" Moharam, and finally Dr. M.J. Soileau, who first got interested me in optics.

Outside of CREOL, I’d like to thank all the friends and family who supported me, in particular my best friend, Alexa La Motte, for whom I’d be too sad without and my archnemesis, Sofia Schlossman, for whom I’d be too happy without. I’d like to thank Cabby.

Lastly, I'd like to thank my mother for all the love and encouragement got me to where I am now and to whom I dedicate this work to.

TABLE OF CONTENTS

LIST OF FIGURES

LIST OF ACRONYMS

CP	circular polarization
CPA	chirped pulse amplification
FWHM	full-width at half-maximum
HOKE	higher-order Kerr effect
HWP	Half-waveplate
LIBS	laser-induced breakdown spectroscopy
LP	linear polarization
MPA	multi-photon absorption
MPI	multi-photon ionization
MTFL	Multi-Terawatt Femtosecond/Filamentation Laser
NA	numerical aperture
NLSE	nonlinear Schrödinger equation
SPM	self-phase modulation
XPM	cross-phase modulation

CHAPTER 1 - FEMTOSECOND FILAMENTATION

1.1 - Introduction

The process of filamentation requires high peak power above 3-10 GW [1] in order for the nonlinear terms to significantly affect propagation. Although laser filamentation was first proposed by Chiao in 1964 [2] and demonstrated in 1966 by Garmire [3], it wasn't until much later in 1995 that the laser technology was advanced enough to produce the peak power necessary to demonstrate filamentation in air [4]. With the more common availability of high-power, ultrashort pulse lasers, the popularity and importance of nonlinear phenomenon such as filamentation has grown. Filamentation is commonly described as a dynamic balance between non-linear Kerr self-focusing and plasma defocusing; causing a core of very high intensity light to propagate without diffracting for many times longer than the Rayleigh length.

Filaments have been studied for a wide variety of applications, including weather control [5], remote sensing with THz (terahertz) or UV radiation [6, 7, 8], long range LIBS (laser-induced breakdown spectroscopy) [9, 10, 11], and transient wave-guiding in air [12, 13, 14]. When filaments are used as a wave-guide, it is generally a structure of many filaments, though a single filament can form a poor quality waveguide [15]. Some examples are based on cylindrical symmetry forming a hollow core wave guide [16], or a rectangular array of filaments [17, 14]. The interaction between these filaments further complicates the already complex and sensitive process of filamentation.

Uncontrolled filaments (no phase or wavefront manipulation) are randomly seeded and defocused by plasma generation and the modulation instabilities of the input beam [18]. Several studies have focused on the control of the multi-filaments by manipulation of various beam parameters [19, 20, 21], including the creation of an engineered filament structure by the introduction of some predetermined phase [22].

This thesis investigates the effects that two filaments or nearly-filamenting beams have on each other with regards to their relative spatial, temporal, and polarization characteristics.

The remainder of chapter 1 summarizes the fundamental processes of filamentation and the properties of filaments. To maintain a relation to the experimental data, only femtosecond filamentation in air at 800 nm will be considered here.

Chapter 2 describes the laser system used as the source; as well as the interferometer design and coding diagnostics developed for these studies.

Chapter 3 describes our results obtained with two interacting beams, either as filaments or as low power sub-critical beams. We describe three regimes. In the first, neither of the two beams being combined are individually capable of forming a filament. Measurements are made on the dependence of spatial separation, temporal delay, and relative polarization orientation between the two beams.

In the second regime a filamenting beam is paired with a sub-critical beam. Measurements of the dependence of spatial separation were done.

Finally in the third regime two filaments are coupled to one another, characterized by their spatial separation.

1.2 - Formation of Filaments

For filamentation in air, high-power, ultrafast (3-10 GW, 40-200 fs [1, 23]) laser sources are required. Short pulses are needed to obtain the high peak power required for the self-focusing effect to arise. The short pulses are also vital so avalanche ionization does not make the plasma overly dense and defocus the beam too early [24].

1.2.1 - Kerr Effect and Self-focusing

The optical Kerr effect describes the change in the refractive index of a material as a function of the intensity of the laser field interacting with the material. The effective index can be described as [23]

$$n(\boldsymbol{r}, t) = n_0 + n_2 I(\boldsymbol{r}, t) \quad (1)$$

where n_0 is the linear refractive, n_2 is the nonlinear refractive index, reported as $n_2 \approx 3 \times 10^{-19}$ cm^2/W for air at 800 nm [25] and $I(\boldsymbol{r}, t)$ describes the intensity of the light field at a specific point in space and time. The nonlinear refractive index depends on the $\chi^{(3)}$of the

propagation medium which is several orders of magnitude lower than $\chi^{(1)}$ ($\sim 10^{-25}\ m^2/V^2$ to $\sim 10^{-4}$ for air, respectively) [26, 27] and thus is negligible in many cases. However, at high enough intensities the nonlinear contribution becomes significant. For a Gaussian beam, the on-axis portion of the beam is higher in intensity and so it experiences a higher index of refraction than the periphery of the beam. This deforms the beam's wave front curvature and causes a focusing effect similar to a positive lens. Figure 1 shows an initially Gaussian profile changing in response to differences of refractive index at different points of the wavefront.

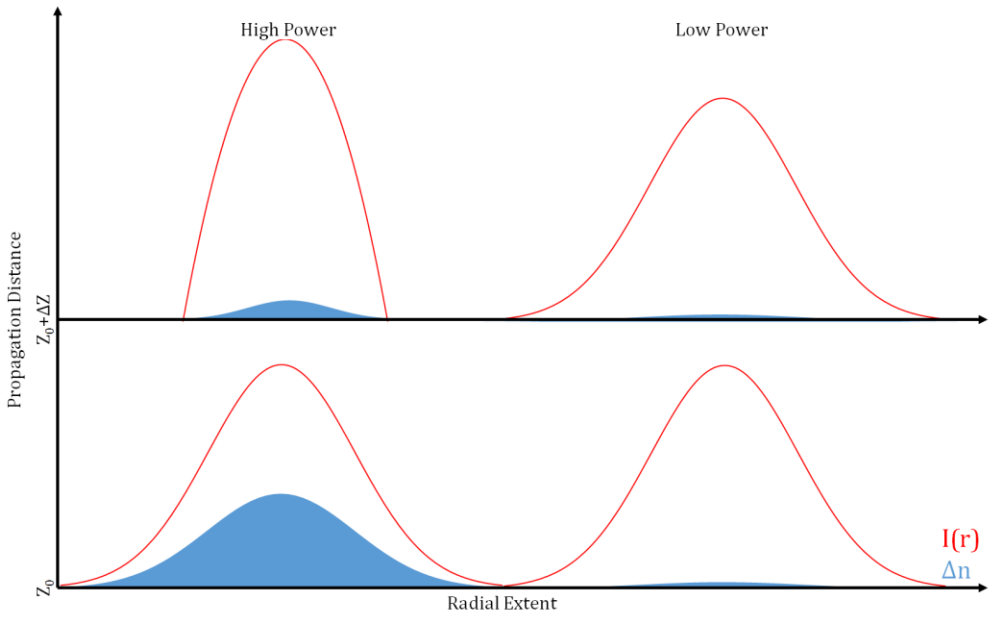

Figure 1 – Diagram illustrating the effect of Kerr self-focusing on waveform deformation via distribution in change of index of refraction.

When the Δn due to Kerr effect causes a stronger focusing effect than the diffraction of the beam due to propagation, Kerr self-focusing [28] occurs and the beam begins to quickly

diminish in size as the Kerr effect causes positive feedback to itself. This process is fundamental to the formation of filaments as well as maintaining the filament structure during propagation.

In the absence of external focusing optics, the focal distance for a CW Gaussian beam undergoing self-focusing is well approximated by [29],

$$z_{sf} \approx \frac{0.367 Z_R}{\sqrt{\left(\sqrt{\frac{P}{P_{cr}}} - 0.852\right)^2 - 0.0219}} \quad (2)$$

where Z_R is the Rayleigh length of the beam, P is the power of the beam, and P_{cr} is the critical power threshold required to form a filament. Z_R and P_{cr} are mathematically defined as [30]

$$Z_R = \frac{\pi \omega_0^2}{\lambda_0} \text{ and } P_{cr} = \alpha \frac{\lambda_0^2}{n_0 n_2} \quad (3)$$

where ω_0 is the Gaussian beam waist at its smallest point, λ_0 is the center wavelength of the beam, α is constant dependent on the input beam profile, and usually ~1.42 [30, 27] for Gaussian beams. In practice, Z_{sf} is generally unrealistically long to use for an indoor laboratory setting, requiring almost 1 km of propagation for a 1 cm wide beam at $P = 1.01 P_{cr}$, so external optics are used to change the self-focusing distance to be

$$\frac{1}{z'_{sf}} = \frac{1}{f} + \frac{1}{z_{sf}} \quad (4)$$

It should be specified that the critical power, P_{cr}, is generally understood as the necessary power for a single pulse to create a single filament. It is important to keep this distinction in mind as the experiments and discussion in chapter 3.1 center around the subversion of the typical values for P_{cr} by combining two sub-critical power pulses to generate a filament.

1.2.2- Plasma Defocusing

Counterbalancing the positive focusing power of the Kerr effect is the defocusing due to plasma generated from the ionization of the propagation medium. Using the Drude model, the modification to the index is given as [23]

$$n \cong n_0 - \frac{\rho(r,t)}{2\rho_{cr}} \quad (5)$$

where n is the plasma index of refraction and $\rho(r,t)$ is the electron density at a particular point in space and time. The two primary processes that dominate the creation of this plasma are multi-photon ionization (MPI) and tunneling ionization. MPI occurs when an electron is freed by absorbing several photons at once. The rate of ionization scales to I^k, with k being the number of photons required to ionize the gas molecules. At $\lambda_0 = 800$ nm, each photon will have ~1.55 eV, so the MPI rate for oxygen, which is the easiest element in air to ionize (requiring ~12 eV), goes as I^8. The tunneling ionization is the process of an electron escaping a potential well which is deformed by strong electric fields. The Keldysh parameter, γ, can be

calculated to determine whether MPI or tunneling ionization is the dominant photo-ionization process.

It is defined as

$$\gamma = \frac{\omega}{e}\sqrt{\frac{m_e U_i n_0 c \varepsilon_0}{I}} \quad (6)$$

where ω is the photon angular frequency, m_e and e the mass and charge of an electron respectively, c is the speed of light in vacuum, and ε_0 is the permittivity of vacuum. MPI dominates if $\gamma \gg 1$, and tunneling ionization dominates if $\gamma \ll 1$. At 800 nm and intensities used for filaments, $\gamma \approx 1.8$ [23, 31]. This indicates that MPI is the dominating ionization process so the MPI ionization rate serves as a good approximation [31].

1.3 - Properties of Filaments

Many properties of filaments have been studied extensively in the literature. The following sections describe only a few effects that are especially pertinent to the experiments described in CHAPTER 3.

1.3.1 – Supercontinuum

The spectrum of a pulse after filamentation will be significantly broader than the initial spectrum of the pulse as new frequency components are generated via Self-Phase Modulation (SPM), self-steepening, and ionization [23]. Typically, the primary cause of this spectral broadening is SPM, the temporal component to the Kerr effect. In normally

dispersive media, the rising edge of the pulse will generate red-shifted frequencies and the trailing edge will generate blue-shifted frequencies. Self-steepening of the pulse causes the high-intensity peak of the pulse to slow down and increases the slope of the trailing edge of the pulse. This leads to an increase in the creation of blue frequencies and asymmetry in the spectrum. The ionization process has also been proven to further blue-shift the spectrum of the pulse [32]. The amount of broadening is related to the length of the filament. Typically, longer filaments have a larger region for non-linear processes to interact with and have broader spectra. Visually, when looking at the cross section of the post-filament beam, the combination of these processes generate a bright, white-light central portion surrounded by rings of color. Figure 2 shows a typical example of the phenomenon.

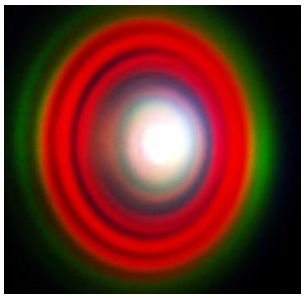

Figure 2 - Example of conical emission by filamentation in a crystal, CaF_2, with 50 μJ pulse and 50 fs duration. [33]

1.3.2 - Terahertz Radiation

The generation of new frequencies from filamentation extends well into the THz range [34]. This is notable due to THz radiation having numerous applications in imaging, sensing, and spectroscopy. Due to large absorption of THz photons from water molecules in air, these

applications are usually restricted to either very short range, high loss, or tight environmental controls in order to operate. However, a filament can be generated at long ranges, creating a THz source near the sample, reducing atmospheric absorption losses.

1.3.3 - Energy Reservoir

The core of the filament continually exchanges energy with the background of energetic photons surrounding it in order to continue to propagate [35]. Energy at the leading edge of the pulse is lost to MPI and defocuses into the reservoir. The trailing edge of the pulse refocuses and draws energy into the filament core from the reservoir and propagation can continue. This cycle of defocusing-focusing can continue for many iterations creating a moving focal point that lasts as long as the filament core can draw enough energy from the reservoir, as illustrated in Figure 3.

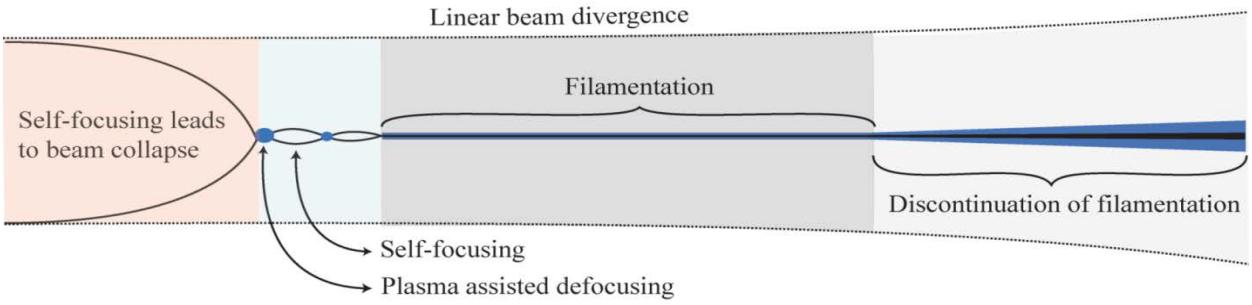

Figure 3 - Illustration of the repeating focusing-defocusing cycle created by dynamic spatial replenishment of the filament. [36]

Restricting or blocking the energy reservoir, the length of the filament is severely reduced or is extinguished [37, 38, 39]. Because of this dynamic spatial replenishment effect between

filament core and reservoir, filaments can be coupled together by interactions between their respective reservoirs. Interesting effects such as attraction, repulsion, and energy transfer can be observed at transverse spatial separations much larger than the dimensions of the filament core [40, 41, 42].

1.3.4 - Filament Plasma and Intensity Clamping

Beyond balancing the self-focusing effect of the filament, the plasma column formed from ionization allows for some intriguing applications, such as microwave or RF (Radio Frequency) guiding. A single filament can guide microwave radiation as a surface wave travelling along the plasma channel of the filament [15, 43]. In theory, arrays of filaments could be organized to mimic a hollow core fiber [16, 44], allowing the microwave or RF radiation to reflect off of the plasma walls of the filaments. The efficiency of the waveguide is controlled by the number and spacing of the filaments as well as the electron density of the plasma. The volume defined by the plasma channels of an array of filaments can even act as a virtual hyperbolic metamaterial with an anisotropic permittivity. Controlling this permittivity, RF radiation can be guided [14, 45].

Another interesting application of the plasma channel is the controlled guiding of electrical discharges. High voltage discharges, such as lightning, can be triggered and guided along the plasma channel of the filament due to the plasma's inherently conductive nature. Compared to spontaneous discharges, a filament reduces the distance threshold for discharge by as much as 50% [46, 47] with guiding capabilities lasting for several microseconds after the pulse [48, 49].

The balance between Kerr self-focusing and plasma defocusing is vital to sustain filamentation. From section 1.2.2, we know the MPI rate has a I^8 dependence. This means plasma density and the strength of the plasma defocusing effect increases dramatically with even small increases of intensity. Once plasma generation begins, the plasma defocusing effect is quickly enhanced to match the Kerr self-focusing term. This prevents further beam collapse and higher intensities which in turn prevents more plasma generation. This negative reinforcement creates a careful balance, so intensities found in the filament are fairly stable and clamped to ceiling value of approximately $4 - 6 \times 10^{13}$ W/cm^2 in air [50], depending on input parameters and conditions. In this range of intensities, the Kerr self-focusing and plasma defocusing reach a dynamic equilibrium. It should be noted that when higher order terms are included in the Kerr effect, nearly plasma-less filaments are predicted to exist [51]. The higher-order Kerr effect (HOKE) model has been heavily debated [52, 53, 54, 55, 56], but regardless indicates an area of weakness in the standard model for filamentation.

Using pulses with higher peak powers to attempt to generate a higher intensity filament will instead generate multiple filaments. Circularly polarized light has been shown to suppress and reduce multi-filamentation [40]. And in theory, a perfectly circularly polarized, radially symmetric beam could completely eliminate multiple filamentation and grant ultra-intense filaments [57, 58]. However, this is not a stable case, not realistically possible to generate as any amount of noise will cause seeds for multiple filaments.

1.3.5 – Polarization

Polarization plays an important part in both the formation, propagation, and coupling of filaments. When compared to circularly polarized (CP) beams, a linearly polarized (LP) beam has the onset for filamentation occurs earlier due to vectorial effects [57], has more efficient photoionization [59], and undergoes more collapse events [60]. There are some conflicting results regarding plasma density and supercontinuum generation, with some groups reporting that the weaker Kerr effect and ionization efficiency cause CP to have suppressed supercontinuum generation and lower plasma density [61, 62, 60] while other groups show enhanced supercontinuum generation and increased plasma density [63, 64]. Elliptically polarized filaments have been shown to anomalous spectral broadening at certain values, related to the molecular character of the media [65].

1.3.5.1– Molecular Alignment

When exposed to electromagnetic fields, molecules will attempt to rotate to align their dipole moment along the direction of the applied field. The dipole moment is proportional to both the polarizability of the molecule and the strength of the electric field. Because the polarizability of a molecule is a second rank tensor, allowing for anisotropic responses along the different axes of the molecule, the molecular alignment process is heavily dependent on beam polarization. Due to the mass of the molecules involved, the time scale for alignment processes is orders of magnitude longer than the typical pulse width of a filamenting beam, so the effects of molecular alignment are muted for single-pulse filaments. However, by sending a earlier pulse to pre-align molecules and timing the delayed pulse molecular

alignment can have varied effects ranging from elongation of the filament length [66], to wavelength tuning and pulse shaping [67], and to birefringence [68, 69, 70]. These effects are typically accomplished by tuning delays relative to molecular revival times, controlling the ellipticity of polarization, or through cross-phase modulation (XPM).

1.3.5.2– Cross-Phase Modulation

In regards to this thesis, XPM is particularly important as it is the mechanism through which intense beams of different wavelengths, directions, or polarizations can couple together.

When two beams (Beam A and Beam B) co-propagate, each beam affects the other's index of refraction. This modifies equation 1 to

$$n(\boldsymbol{r},t) = n_0 + n_2 I_A(\boldsymbol{r},t) + n_2^{XPM} I_B(\boldsymbol{r},t) \tag{7}$$

where $n_2^{XPM} I_B(r,t)$ is the change in index experienced by Beam A due to Beam B from XPM. This change is polarization dependent and can be broken down in terms of the third order electric susceptibility tensor for the propagation media [24].

$$n_2^{XPM} = \Delta n_{\parallel} + \Delta n_{\perp} \tag{8}$$

Where $\Delta n_{\parallel}$ and $\Delta n_{\perp}$ are the change in refractive index corresponding to the polarization components of Beam B that lie parallel and perpendicular to Beam A's polarization, respectively.

$$\Delta n_{\parallel} = \frac{3\varepsilon_0}{4n_0}\mathrm{Re}\left(\chi^{(3)}_{xxxx}\right) \tag{9}$$

$$\Delta n_{\perp} = \frac{3\varepsilon_0}{4n_0} Re\left(\chi^{(3)}_{xxxx}\right) \tag{10}$$

Though forth-rank tensor in general, the third-order electric susceptibility can be represented as a scalar quantity for individual linear polarizations in an isotropic medium such as air. In general, the parallel and perpendicular components are not equal and will cause birefringence in the filament as it propagates, causing spatio-temporal reshaping of the filamenting pulse [71].

1.4 - Multi-Filamentation and its Engineering

As discussed in the previous section, trying to inject more power into a beam will instead cause the beam to break apart into multiple filaments when the total power is much greater than the critical power. Each of the new, branching filaments carrying a power $P_{fil} \cong \frac{\pi^2 P_{cr}}{4}$ [72]. The close proximity of two or more filaments gives rise to several new phenomenon, such as filament interference, competition and cooperation [73]. In one case, the parent filaments arise from hot spots in the noise. The conical rings and background quasi-plane wave surrounding each filament interfere. Areas of constructive interference will attempt to also self-focus and create new filaments [74, 75]. If the hot spots are sufficiently far apart,

the interference will be too weak to form intense enough hot spots for new filaments. Because each of the filaments are attempting to draw from the same source, this competition causes all of filaments to have an energy deficiency and create fewer total filaments. However, by simply reducing the initial beam size or otherwise forcing the initial hot spots closer together a second case occurs. The interference creates strong enough secondary hot spots to form "daughter" filaments. The filaments work together to collectively draw in energy from the background reservoir as a single filament would. This allows for more numerous filaments, fully mature filaments to be formed [73, 76, 75].

Without external control, the initial location of the hot spots in the beam arises from random noise, so even on a shot-to-shot basis it is difficult to predict the specific properties of the filaments. There have been numerous attempts at controlling the initial conditions of the beam in such a way so as to create specific patterns of multiple filaments. These engineered filaments can be created by simply tilting a focusing lens and applying astigmatism to the beam [77], controlling the beam ellipticity [21], or by applying a pre-determined phase distribution to the beam [78, 79, 80]. In the case of having a phase distribution, the specific phase relations between the filaments can be exploited to exhibit properties of energy exchange, attraction, and repulsion, allowing the filaments to rotate in space as they propagate, similar to the case of two individual filaments coupling together [22, 40]. Figure 4 shows an example rotating, helical filaments. The helical beams were generated by placing a complex coaxial vortex plate in series with a pair of coaxially aligned Fresnel axicons with diffraction angles $\beta_i = 0.0375°$ and $\beta_o = 0.06525°$.

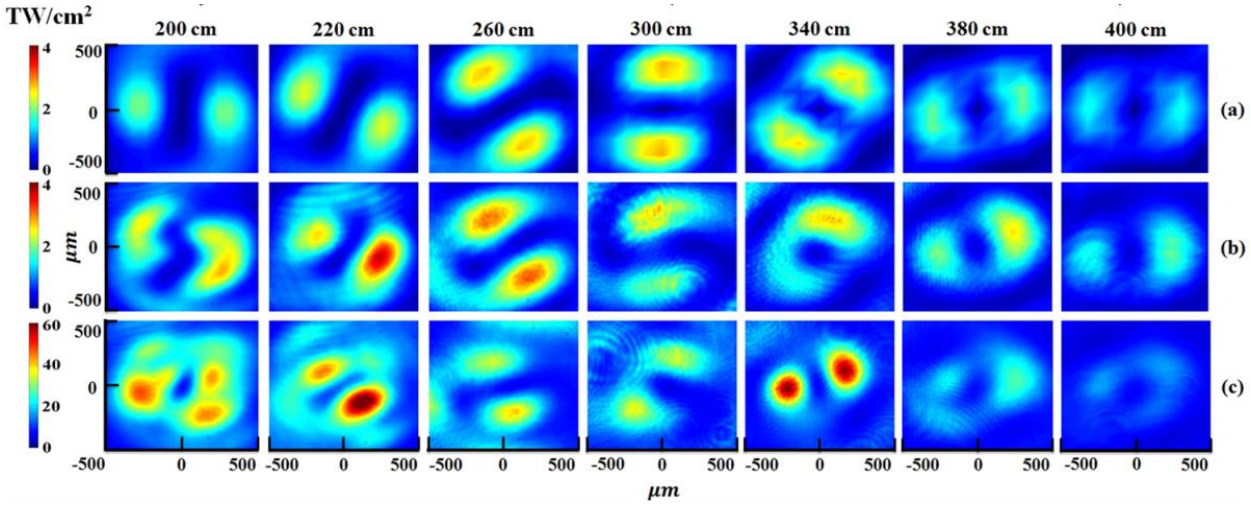

Figure 4 - Helical beam transverse profiles as a function of propagation distance, simulated (a), measured for 135 μJ pulses (b) and 11.5 mJ pulses (c). (~50 fs pulse width, f=2.1 m) [80].

CHAPTER 2 – EXPERIMENTAL DESIGN

2.1 – Laser

The laser used in this study was the MTFL (Multi-Terawatt Femtosecond Laser) in the Laser Plasma Laboratory in the Townes Laser Institute/CREOL. This system is a Ti:Sapphire chirped pulse amplification (CPA) system capable of delivering 40-50 fs pulses with up to 470 mJ of energy at 10 Hz repetition rate or 1 mJ pulses at 1 kHz repetition rate. Figure 5 represents the layout of the laser system schematically. The oscillator is a Spectra-Physics Tsunami, Kerr-lens passive mode-locked Ti:sapphire laser, pumped by a Spectra-Physics Millenia V CW at 532 nm with powers between 5-25 W. The output of the oscillator is a train of ~35 fs, 800 nm pulses with an average power of 330 mW at 74 MHz. The pulses are then stretched with an in-house designed pulse stretcher using an Offner type configuration. After two passes, the pulses are stretched to ~450 ps (picoseconds). Pulses are then passed through a Fastlite dazzler, which is an acousto-optic programmable dispersive filter. The dazzler is used to control the spectral phase and amplitude of the pulse and counter gain narrowing effects in the amplification stages of the system. The dazzler is controlled in a feedback loop through a Fastlite Wizzler placed at the output of the laser, using self-referenced spectral interferometry. The modified pulses are used to seed the regenerative amplifier. The regenerative amplifier is a modified Spectra-Physics Spitfire system and is double side pumped by a Spectra-Physics Evolution-30 laser emitting 20 W of 527 nm pulses at 1 kHz. The entry and ejection from the regenerative amplifier is controlled by two Pockels cells. Each round trip takes ~10 ns and after ~30 round trips the pulse is amplified to ~2.5 mJ. The pulses are passed through a spatial filter to clean the beam profile before entering

the pre-amplifier stage. The pre-amplifier is a six-pass bowtie amplifier with the Ti:sapphire crystal double side pumped by a Spectra-Physics Quanta-ray Pro 290 with ~750 mJ pulses at 532 nm. The output pulses are amplified from ~2.5 mJ to ~160 mJ. The pulses are passed through a spatial filter with approximately 70% transmission for an output energy of ~112 mJ. After the spatial filter, there is a motorized flip mirror that will send the pulses to either the final amplifier pump for the full energy output or through an expanding telescope and attenuator to the high energy compressor. The final amplifier is a three-pass bowtie amplifier with the Ti:sapphire crystal double side pumped by a Continuum Powerlite DLS with ~2 J pulses at 532 nm. The final amplifier will amplify the ~112 mJ seed pulses to ~750 mJ. The pulses then enter the high energy Treacy compressor [81] after the final amplifier stage or if the flip mirror before the final amplifier is in the up position. The compressor consists of two gratings and a corner reflector that counter the dispersion introduced by the Offner stretcher and produce the final output pulses with 40-50 fs pulsewidth at either ~470 mJ or 16 mJ .

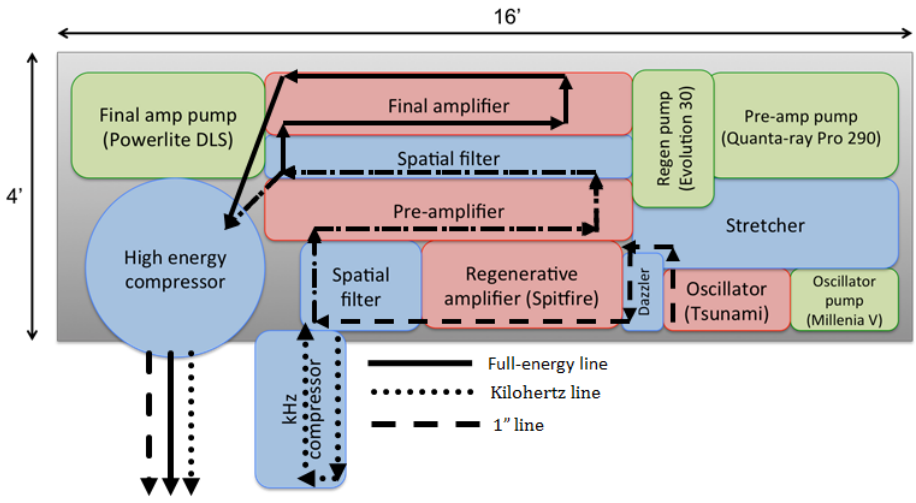

Figure 5 - Schematic layout of the MTFL system on a 16' x 4' optical table. Full-energy line: 10 Hz repetition rate, <45 fs pulse duration, 470 mJ pulse energy, Kilohertz line: 1 kHz repetition rate, 50 fs pulse duration, 1 mJ pulse energy, and 1" line: 10 Hz repetition rate, <45 fs pulse duration, 10 mJ pulse energy [65].

2.2 – Experimental Setup

In order to characterize the interactions between two beams, a versatile system capable of independent control of beam location, delay and polarization is needed. The interferometer used for this study, Figure 6, was designed to separate and recombine the beams with controllable spatial and temporal separation with a resolution of 25.4 micrometers (μm) and ~0.1 femtoseconds (fs), respectively. The initial half-wave plate (HWP) is used to rotate the initial horizontal polarization of the beam to vertical to allow for maximum transmission through the beamsplitters. The pair of mirrors located after the first beamsplitter are mounted on a programmable motorized stage to create the temporal delay relative to the static arm. Both the second beamsplitter and the active arm's lens are mounted on a manual stage to control the spatial separation between the beams. Both lenses have a focal distance of 5 meters. The beams were aligned spatially and temporally to optimize pulse overlap. The spatial overlap of the two beams was done by looking at the beam profiles along the propagation using a Charge-Coupled Device (CCD) camera (The Imaging Source DMK72BUC02). Using the beam profiles, the beams are measured to be collinear to each other within < 0.5 μrad. The beams were temporally aligned by adjusting the delay to find the zero delay to eliminate fringes in the combined spectrum. A second HWP was used (see Section 3.1.2) after the first beamsplitter to rotate the polarization of one arm relative to the other. Additional glass slides were used to compensate for changes in transmission, due to polarization change, at the second beamsplitter. Self-referenced spectral interferometry measurements find the additional dispersion from the added elements to be $<<$ 1 fs and are considered negligible.

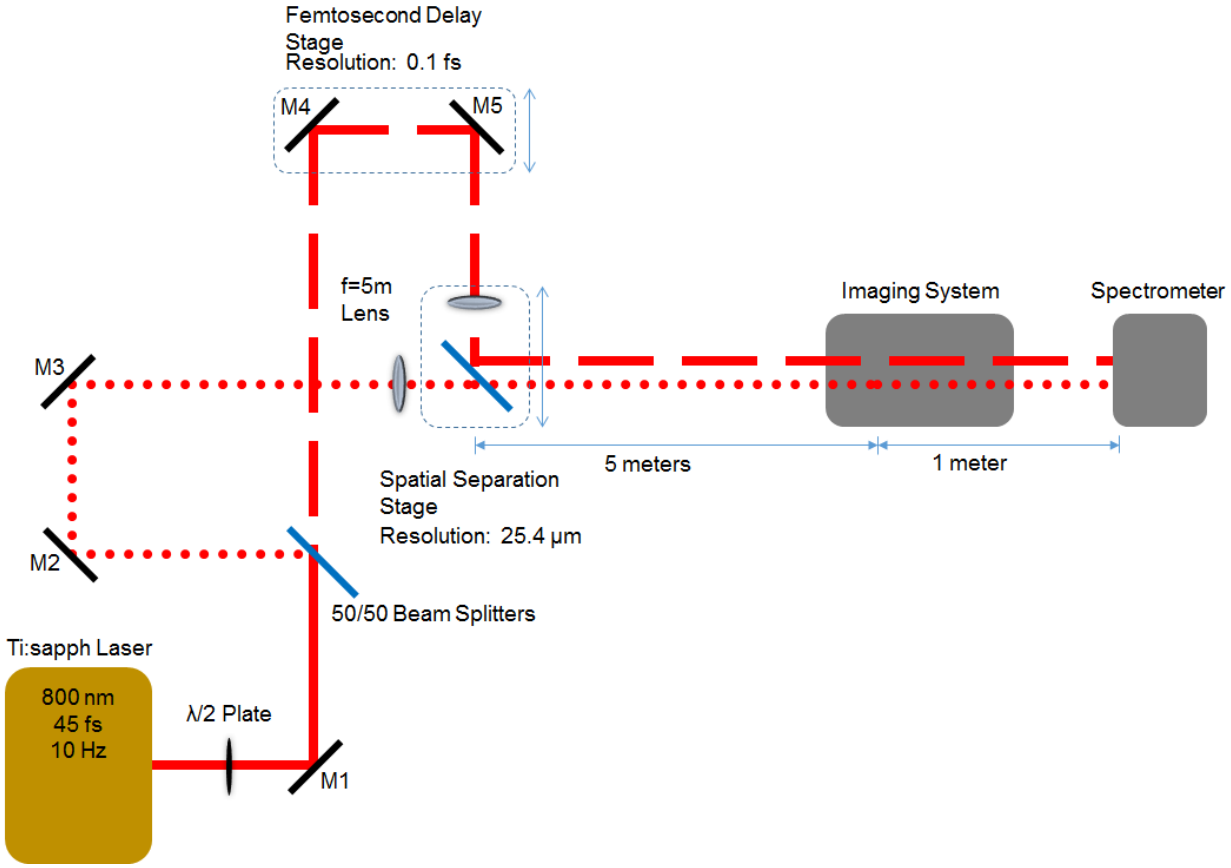

Figure 6 - Illustrated diagram of interferometer set-up used to split and combine beams.

With the system shown in Figure 6, the beam profile and spectrum are recorded for each initial beam separation to characterize the combined beams. The system used to image the beam profiles (Figure 7) was composed of a series of grazing incidence uncoated fused silica wedges as an attenuator. The large angle of incidence (AOI) relative to the surface normal prevents surface damage from the high intensity filaments. The low reflectivity attenuates the beam intensity by a factor of 10^7. This allows the CCD to safely image the filament beam profile with a lens (f = 100 mm).

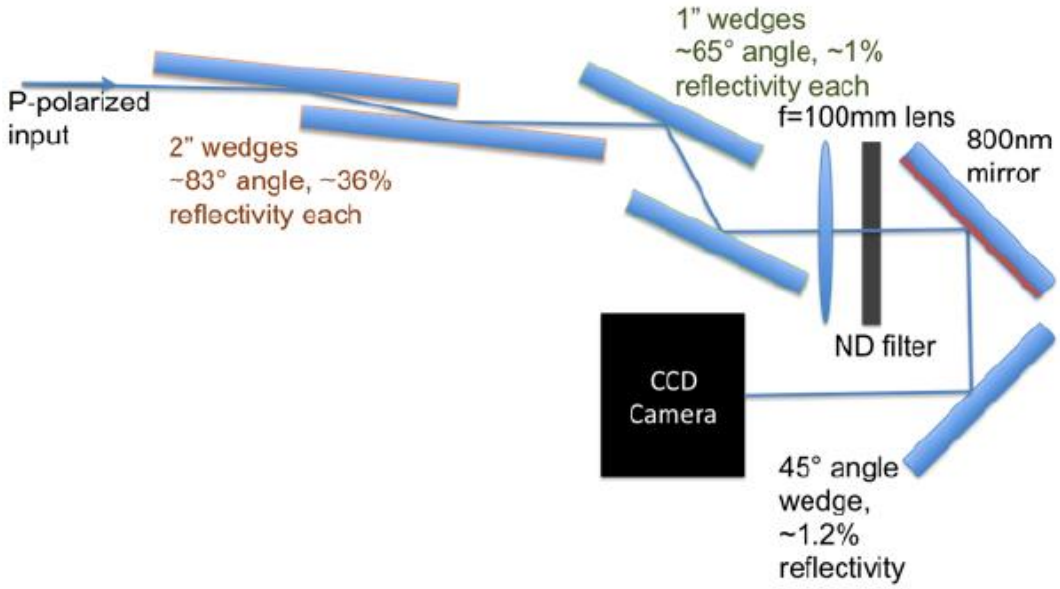

Figure 7 - Schematic of the grazing incidence imaging system [65].

2.3 – Diagnostics

Laser filaments and filament interaction are controlled by many complex, nonlinear processes. In order to better understand the interplay among the various physical processes involved in filamentation, a numerical simulation was developed to accurately described filament propagation. The in-house Matlab simulator, developed by Khan Lim [65], solves the expanded version of the NLSE (Non-Linear Schrödinger Equation), represented by Equation 11, via the split-step method. This approach has been used in several other studies [23, 35, 82, 60].

$$\frac{\partial \varepsilon}{\partial z} = \frac{i}{2k}\nabla_{\perp}^{2}\varepsilon - i\frac{k''}{2}\frac{\partial^{2}\varepsilon}{\partial t^{2}} + ik_0 n_2(1-f)|\varepsilon|^{2}\varepsilon + ik_0 n_2 f\left[\int_{-\infty}^{t} R(t-t')|\varepsilon(t')|^{2}\,dt'\right]\varepsilon \qquad (11)$$
$$-\frac{\sigma}{2}(1+i\omega_0\tau_c)\rho\varepsilon - \frac{\beta_K}{2}|\varepsilon|^{2K-2}\left(1-\frac{\rho}{\rho_{nt}}\right)\varepsilon$$

Equation 11 describes pulses moving in their group velocity frame and characterized by their FWHM, τ_p. The terms on the right hand side represent the effects of diffraction, group velocity dispersion, k", instantaneous Kerr effect, delayed Raman-Kerr effect, absorption and defocusing from the plasma, and MPI losses. The f factor splits the contributions from the Kerr self-focusing effect in to the instantaneous electronic effect and the delay molecular Raman effect. The function $R(t) = \frac{\Gamma^2-\omega_R^2}{\omega_R^2}\exp(-\Gamma t)\sin\omega_R t$ describes the molecular response of the medium where Γ^{-1} is the molecular response time and ω_R is the rotational frequency. In air, $\Gamma = \frac{1}{70}fs$ and $\omega_R = 16\times10^{12}s^{-1}$ [23, 83]. The plasma term accounts for both absorption (real part) and defocusing (imaginary part). The coefficient σ represents the cross section for inverse Bremsstrahlung. $\sigma = \frac{k_0}{n_0\rho_c}\frac{\omega_0\tau_c}{(1+\omega_0^2\tau_c^2)} \approx 5.6\times10^{-20}$ cm^2 [23]. τ_c is the electron collision time (~350 fs in air) and ρ_c is the critical plasma density. For plasma density values $> \rho_c$, the plasma becomes opaque to the laser. $\rho_c = \epsilon_0 m_e\left(\frac{2\pi c}{e\lambda_0}\right)^2 \approx 1.7\times10^{21}$ cm^{-3} for 800 nm [23]. ϵ_0 is the permittivity of vacuum, m_e and e the mass and charge of an electron, λ_0 is the central wavelength in vacuum, and c the speed of light in vacuum. β_K is the MPI coefficient, given by $\beta_K = K\hbar\omega_0\rho_{nt}\sigma_K$. Because MPI rates are primarily driven by ionization from oxygen molecules, $K = 8$. $\beta_8 \cong 4.25\times10^{-98}\ {cm^{13}}/{W^7}$ with center frequency of $\omega_0 = 2.36\times10^{15}\ Hz$,neutral density $\rho_{nt} = 5.4\times10^{18}\ cm^{-3}$, and $\sigma_K = 2.88\times10^{-99}\ s^{-1}{cm^{16}}/{W^8}$ [72]. Equation 11, combined with the evolution of the electron density (Eq. 12), forms the core components of the numerical simulation.

$$\frac{\partial \rho}{\partial t} = \sigma_K I^K (\rho_{nt} - \rho) + \frac{\sigma}{U_i} \rho I \tag{12}$$

The terms on the right hand side represent *K*-photon MPI and avalanche ionization. σ_K is the *K*-photon ionization cross section, I^K is the intensity to the K-th power, ρ_{nt} the density of neutrals in the medium and σ is the cross section for inverse Bremsstrahlung. U_i is the gap potential of the ionizing medium (12.1eV for oxygen [72]).

The numerical simulation is performed in (2D+1) dimensions in terms of radial distance from the axis and local time with respect to the pulse. To simplify the problem, the beam is assumed to be axially symmetric and group velocity is fixed. In Figure 8, the workflow of the simulation is diagrammatically shown and in-depth details of each step and subsequent sub-steps, can be found in [65]. *N* represents the collection of all nonlinear terms together and Δz represents the step size along the direction of propagation. Δz is adaptive such that $|N\Delta z| < 0.01$ in order to capture sharp spatial and temporal features that arise from filamentation.

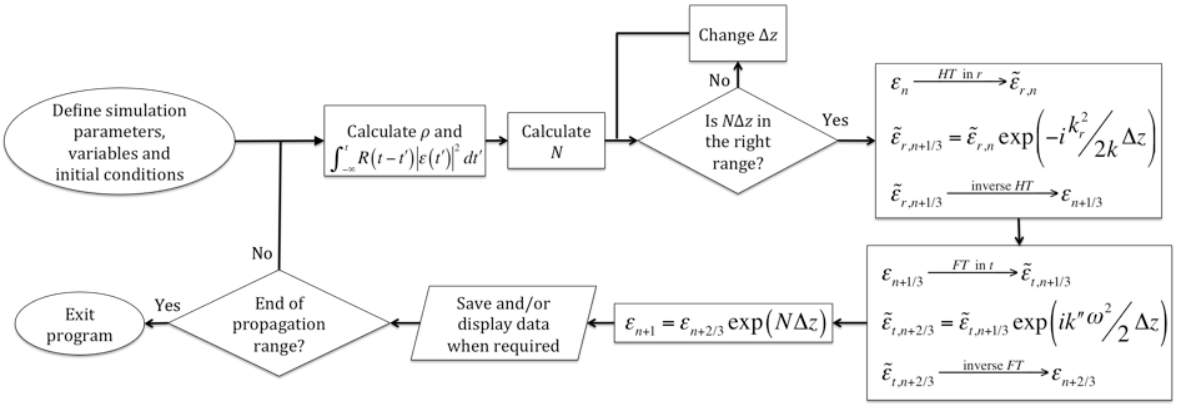

Figure 8 - Flowchart of filament simulation program based on solving the NLSE by the split-step method [65].

Post processing of the experimental data was also handled with a set of Matlab codes that perform background subtraction, averaging, and normalization to all data sets. Beam intensity profiles are obtained via the Radon transform, a series of integrals done in straight lines across the image [84], at angles taken to coincide with the x- and y-axes orthogonal to the direction of propagation. The initial spectrum of the laser output is subtracted from the measurements of spectra so that only broadening and enhancement of spectral intensity are shown.

CHAPTER 3– FORMATION AND COUPLING OF FILAMENTS

In this chapter, the beams were characterized by their intensity beam profile, spectrum, and conical emission. These beam qualities were measured as a function of several input parameters (initial separation, temporal delay, and relative polarization). From these observations, the dependence of coupling between combined beams or filaments can be determined. This was done in several different energy regimes, two sub-critical pulses, one sub-critical pulse with one filament, and two filaments.

3.1 – Coupling between Two Sub-critical Beams

For the laser source used in these studies, see Section 2.1, the threshold pulse energy for a single filament is consistently measured at ~1.33 mJ. The threshold was determined by increasing the input pulse energy until every shot shows a broadened spectrum and distinct conical emission that indicates filamentation, shown in Figure 9.

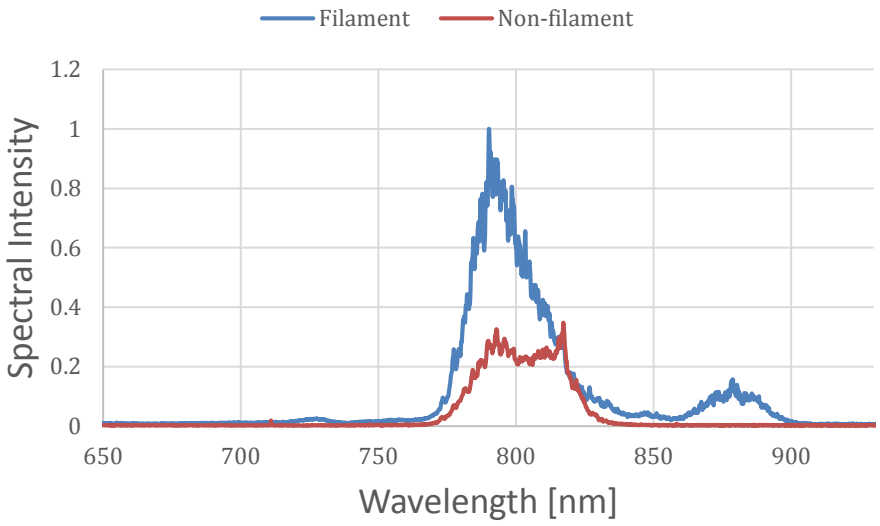

Figure 9 - Example of filamenting spectrum (blue) compared to a sub-critical spectrum (red).

In this set of experiments, two sub-critical beams are combined and the resulting beam profiles and spectra are measured. The experimental set-up used is as described in section 2.2. The resulting beam profiles were measured at the geometric focus and the spectra were collected via an optical fiber one meter after the geometric focus. For all data sets, each pulse had an energy between 0.8 to 1 mJ to prevent individual filamentation.

3.1.1 – Spatial Separation

The two beams are separated in the transverse direction by adjusting the position of the spatial separation stage in increments of 25.4 μm and compensating for the difference in optical path length with the femtosecond delay stage. The reference beam has an average pulse energy of 0.96 mJ and the adjustable beam has an average pulse energy of 0.89 mJ. The measurements of the peak locations as the initial separation between the two beams are decreased (Figure 10a), show a clear attraction between them. At ~1370 μm initial separation, the attraction between the two beams becomes significant and the center of the beams move nonlinearly as the two beams are brought closer to each other. It should be noted that the peak locations from 1350-1200 μm of the adjustable beam are influenced by beam clipping on the imaging wedges. Extrapolating from data points where the trend between the initial and measured beam separation is more linear (initial separation of 1250-1000 μm) indicates a negligible attraction between the two beams. Between 660 μm and 330 μm is a region of high instability in beam location. Below 330 μm initial beam separation, the two beams are indistinguishable from one another and generate a single filament.

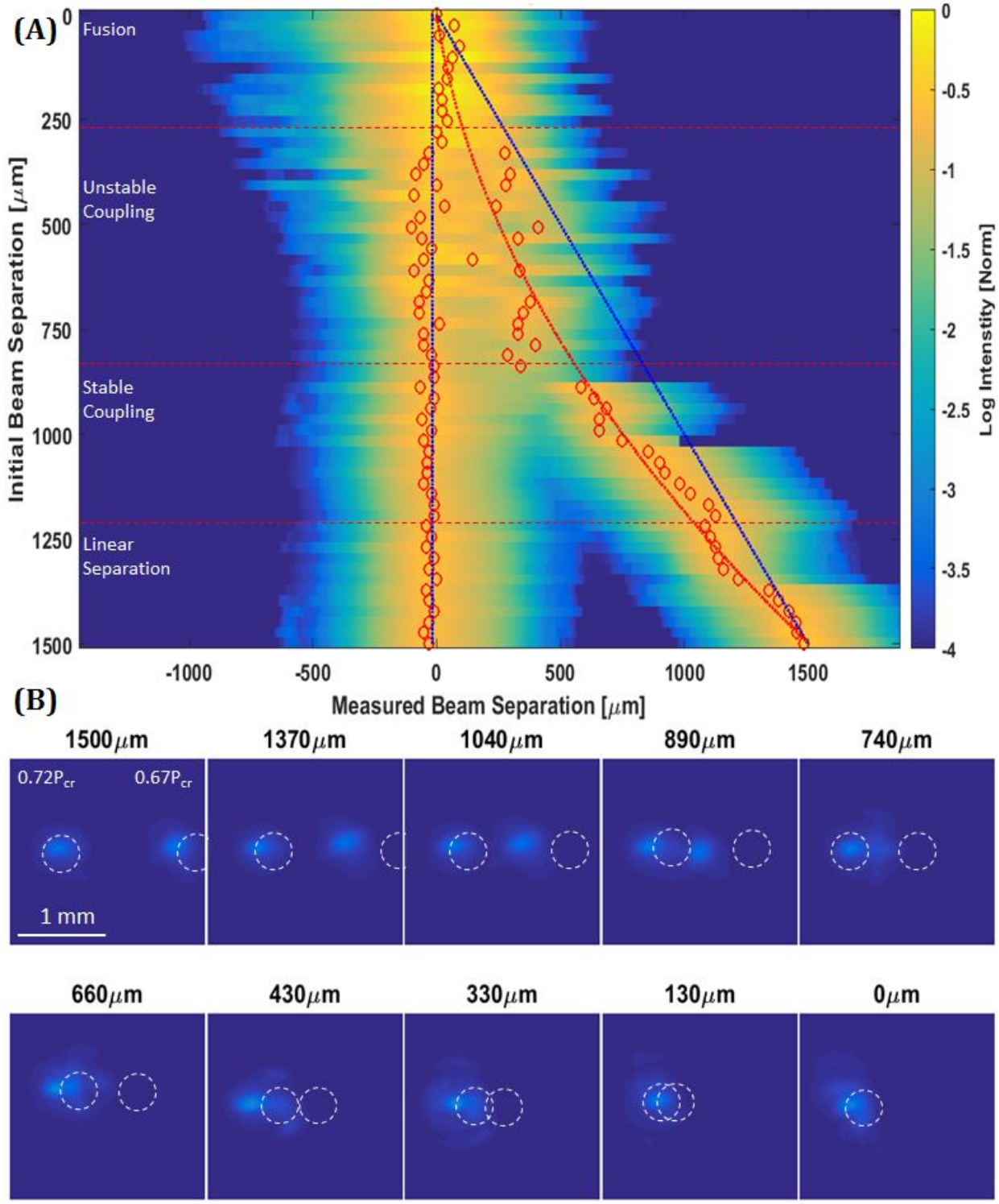

Figure 10 – (a) Beam intensity profiles at various separations. Red circles denote locations of intensity peaks. Beam A is shown on the left, and Beam B on the right. (b) Selected cross-sectional beam profiles at various initial beam separations, circles denote initial location of the beams.

Figure 10b shows a cross-sectional view of the beams as separation decreases and the beams strong attraction from the cross-Kerr effect. The deflection of the measured beam locations (red circles) relative to the initial beam locations (blue lines) is measured. The red line on Figure 10 represents a fit of the centroids of Beam B. The fit shows that the deflection has a quadratic dependence on initial beam separation.

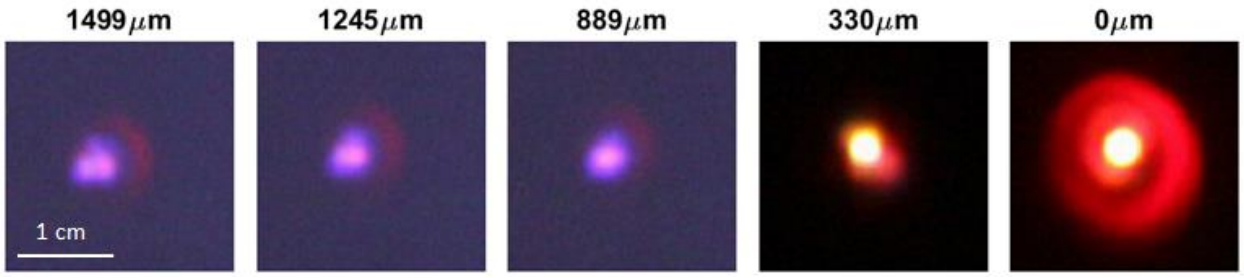

Figure 11 – Conical emission profiles after six meters of propagation from the point of beam combining. Images before 990 micrometers are exposed for three times longer than later images.

Supercontinuum is visible even up to separations of ~1500 μm (Figure 11). This indicates the existence of nonlinear effects not seen during propagation of the individual, sub-critical beams. The consistent asymmetry of the conical emission profile in the large separation regime (>990 μm) indicates that the more energetic Beam A (0.96 mJ) attracts and draws energy from the less energetic Beam B (0.89 mJ) in order to generate a filament. The spectral broadening in Figure 12 confirms energy transfer up to 1.5 mm. Figure 12b shows less than 10% decrease in peak spectral intensity between complete spatial overlap (blue) and 1.5 mm of initial beam separation (green). Additional peaks are seen in the spectra in both the red and blue sides. These peaks are likely due to spatio-temporal reshaping of the pulse from X-wave generation and propagation [71]. However, without angularly resolved

measurements of spectra or other additional measurements, the specific underlying gain mechanism cannot be determined. The small peak in the blue disappears entirely at large initial beam separations. At large separations the peak in the red shifts closer to the central wavelength, though it increases in intensity. This may indicate that the process that causes the peaks to shift is a self-seeding effect, similar to continuous Raman self-frequency down shifts in fibers [24].

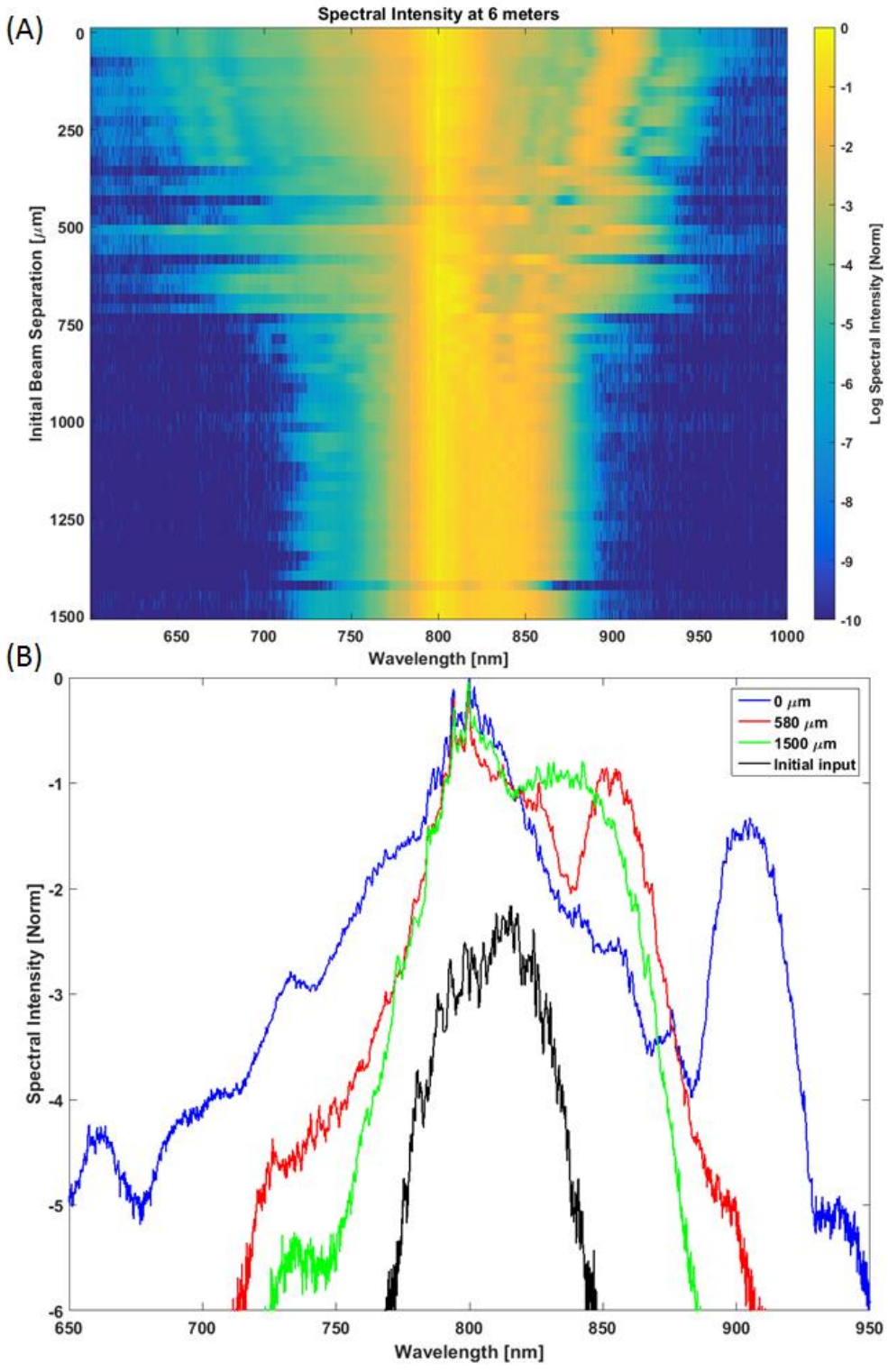

Figure 12 - (a) Spectral intensity of combined beams as a function of initial beam separation. (b) Select spectra at 0 μm (blue), 580 μm (red), and 1500 μm (green) initial beam separation compared to spectrum of a single beam (black) before combination.

3.1.2– Relative Polarization and Temporal Shift

As discussed in section 1.3.5.2, polarization plays a large part in how one beam affects another. Previous reports show polarization rotation [69], phase retardation [68], and complex interaction between XPM induced Kerr-induced attraction and plasma cross-defocusing [85]. In this study, two beams are spatially overlapped and one is delayed in time. Both beams are initially linearly, vertically, polarized. The polarization of one of the beams is rotated with a HWP; up to 180° difference in polarization orientation, for each delay. Positive delay indicates earlier time for the beam that rotates in polarization. The measured experimental spectra are compared to simulation data generated using the numerical model described in section 2.3. The effect of delayed molecular revivals (ps time scale) are not observed due to the smaller time delays considered in these experiments. Figure 13 shows the experimental setup modified slightly with the addition of a second HWP. Spectra was measured, similar to Section 3.1.1, for selected time delays and different relative polarizations between the two beams.

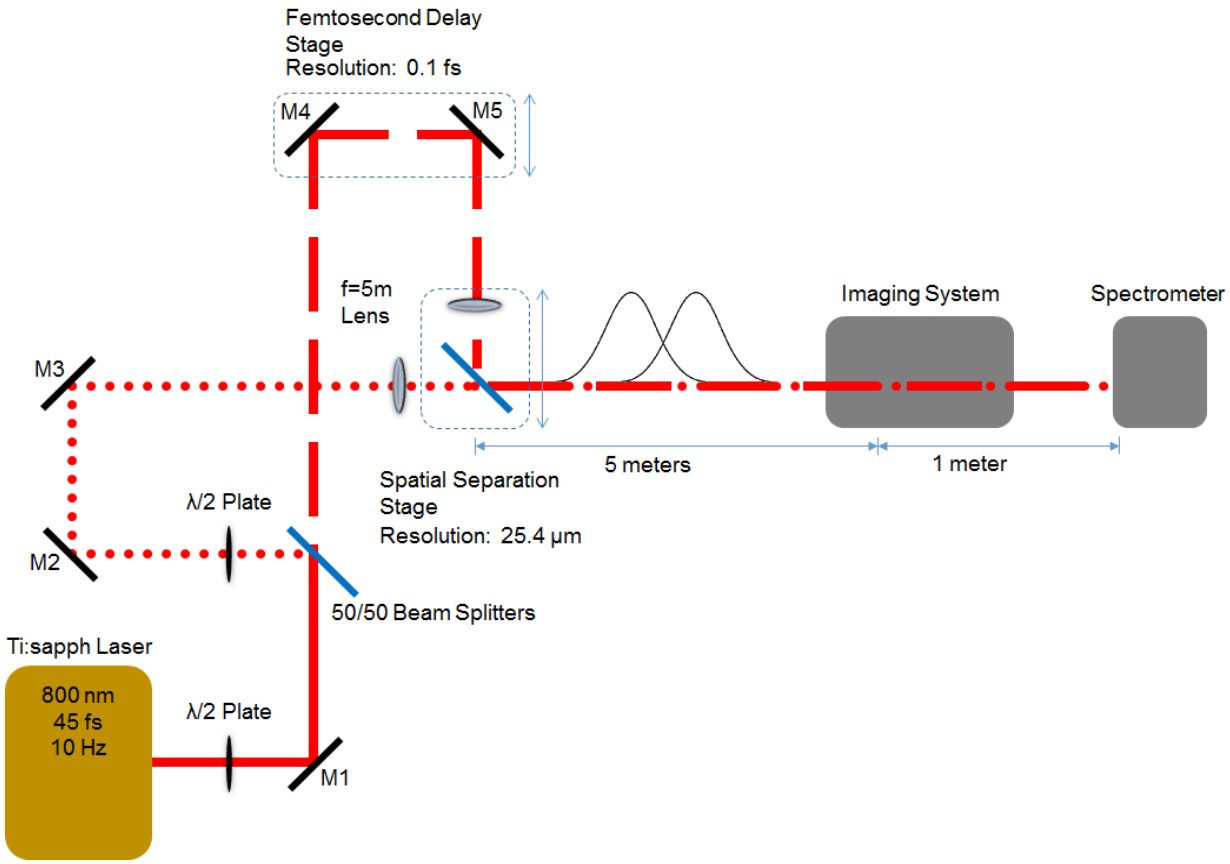

Figure 13 - Schematic of the modified setup.

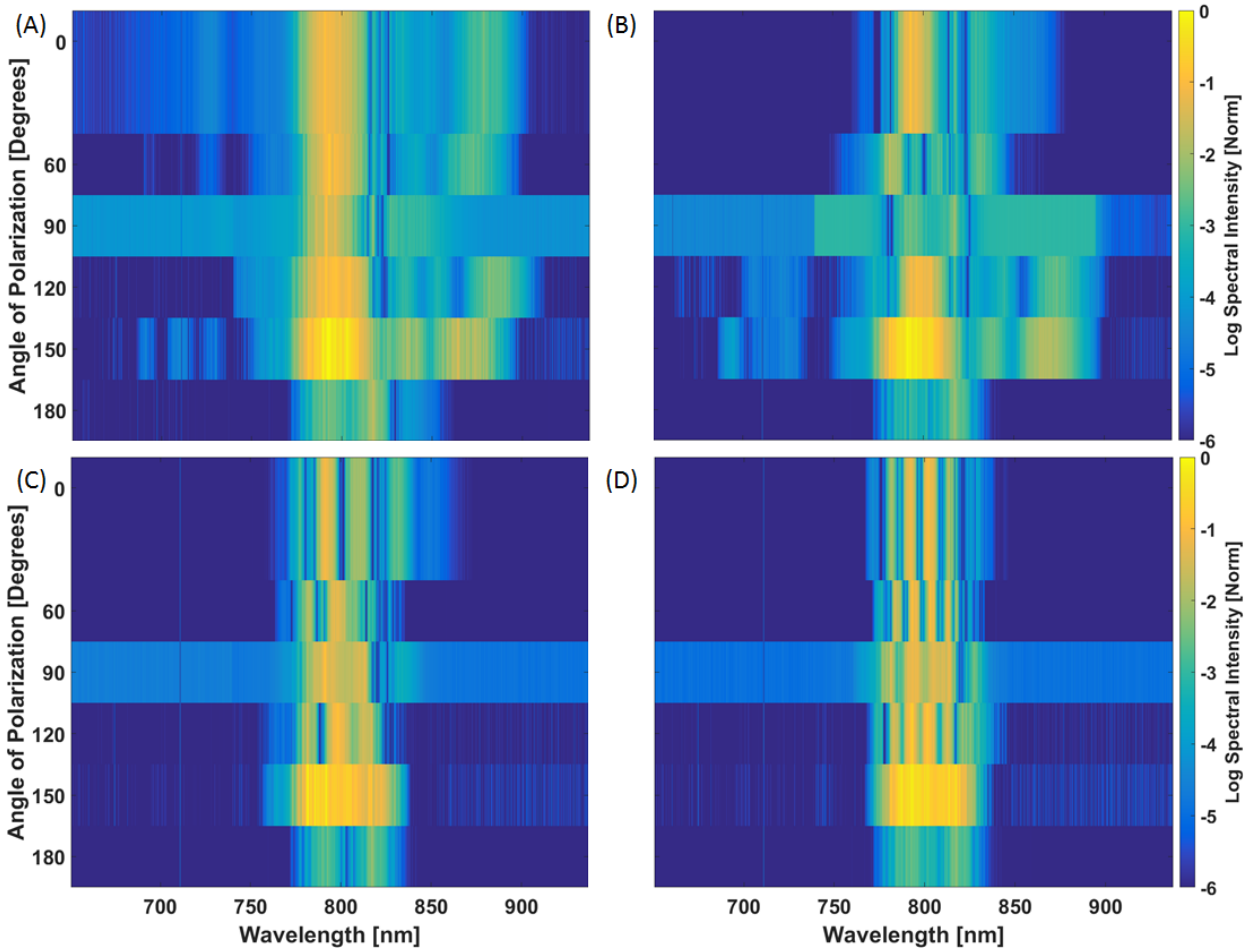

Figure 14 – Experimental spectra of combined beams at (a) 0 fs, (b) 20 fs, (c) 50 fs, and (d) 100 fs delay. Angle of polarization is relative to the vertical.

To highlight the nonlinear features and increase fringe contrast, measured spectra shown in Figure 14, has been corrected for the input spectrum. Figure 13a shows a large broadening with secondary peaks in both the blue and red side of the spectrum at 0 angle of polarization difference. This spectral broadening is an evidence of filamentation when the delay and polarization are well overlapped. At 100 fs delay and beyond (Fig. 13d), the pulses are separated further than their FWHM (~48-50 fs), and the nonlinear effects are no longer strong enough to form a filament from the combined beams. In the cases where a filament is

generated (Fig.13 a-c), spectral broadening is largely increased at orthogonal polarizations and spectral intensity is at a maximum at 150° angle of polarization difference. At 180° angle of polarization, destructive interference dominates, preventing filament generation. This indicates optimal coupling between the beams when they are at 150° relative polarization difference to one another. The mechanism for the enhanced spectral broadening at partially destructively interfering polarizations is not totally understood at this point and requires further investigations into the phenomenon.

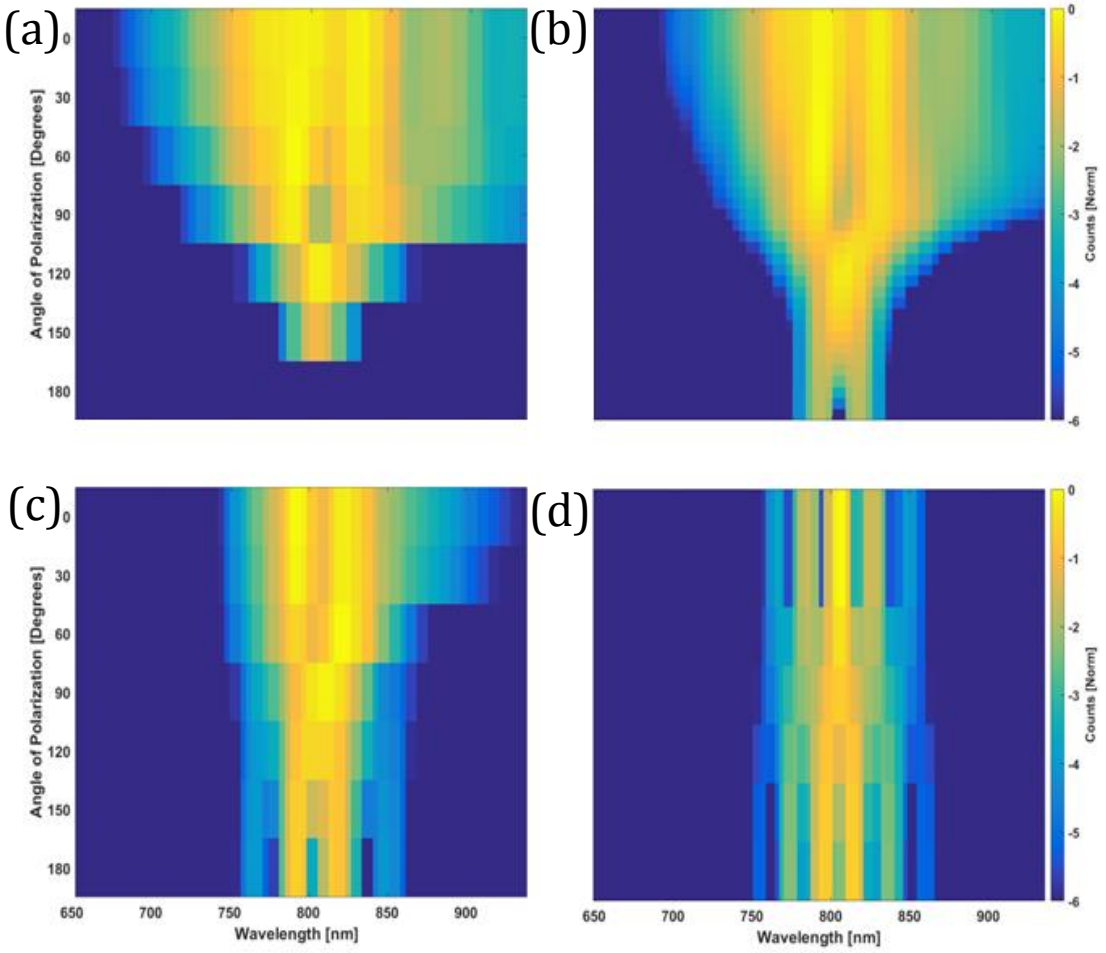

Figure 15 - Simulated spectra of combined beams at (a) 0 fs, (b) 20 fs, (c) 50 fs, and (d) 100 fs delay. Angle of polarization is relative to the vertical.

Figure 15 represents the simulated spectra for the same conditions as in the experiments (Figure 14). There is a good agreement in the estimation of spectral peak features, with less than 2.5% error in peak locations in all cases. However, the simulations predict a steady decrease in both spectral broadening and intensity, unlike the experimental case. Given the success of the numerical code in predicting spectral peak features, broadening, and other polarization-dependent phenomenon [65], it is unlikely that the mismatch is due to errors in the coding but rather from processes not taken into account in the model. The code

supports spectral broadening from SPM, XPM, self-steepening, effective three wave mixing, and molecular alignment [65], which are the common contributors to spectral broadening. The failure of the simulation to predict the irregular broadening indicates that these processes are not explicitly responsible.

3.2– Coupling between a Filament and a Sub-critical Beam

In this set of experiments, a beam with sufficient energy to generate a filament ($E_{pulse} > 1.3\ mJ$) co-propagates with a beam with energy below the threshold for filamentation (~1.3mJ). The experimental set up is the same as described in chapter 2.2. The beam intensity profiles, post-filament spectra, and conical emission are recorded. The beam profiles were measured at the geometric focus and the spectra and conical emission images were collected via an optical fiber one meter after the geometric focus.

3.2.1 – Spatial Separation

Similar to section 3.1.1, the beams are separated in the transverse direction by adjusting the spatial separation stage. Differently than section 3.1.1, the adjustable beam (1.42 mJ) is capable of generating a filament on its own while the static beam (1.01 mJ) is below the threshold for filament generation.

From Figure 16, it can be seen that there is attraction between the two beams; most notably the sub-critical beam (left beam in Figure 16) is absorbed entirely by the filamenting beam (right beam on Figure 16). The dynamic filament experiences mild deflection (>20 μm) away from its initial beam separation (blue line).

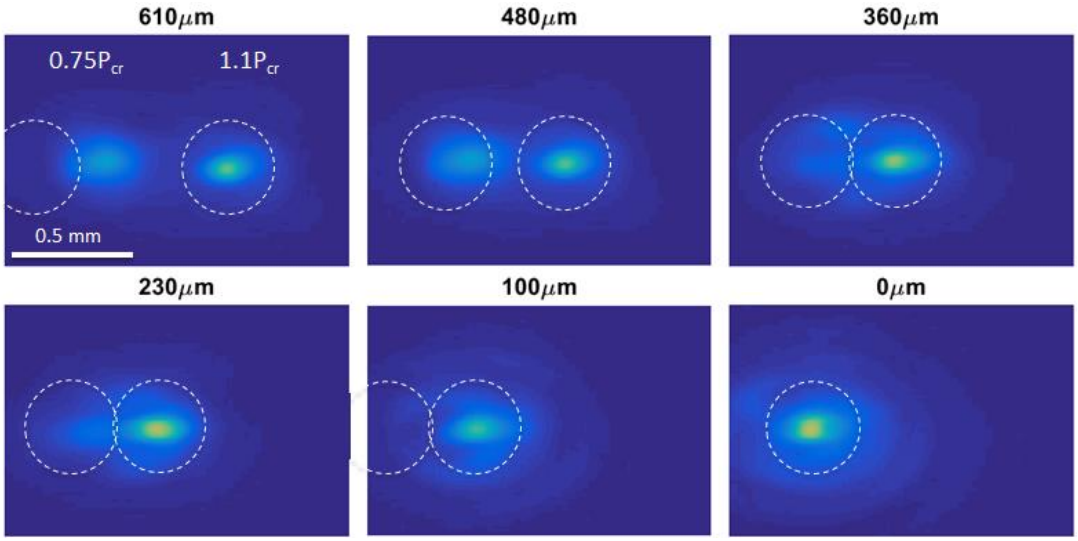

Figure 16 – (a) Beam intensity profiles of combined filament/non-filament beam after 5 meters of propagation from beam combining point. Red circles denote peak locations. Left, static sub-critical beam (1.01 mJ); Right, filament (1.42 mJ). (b) Selected cross-sectional beam profiles at various initial beam separations.

From Figure 17, there is attraction and fusion at ~480 μm of initial beam separation. The two beams initially have a relatively low intensity. As the sub-critical beam is attracted to the filament, the filament's intensity is enhanced and the sub-critical beam becomes a shoulder.

Finally, at complete spatial overlap there is a ~60% increase of intensity and a definite Townes-like profile.

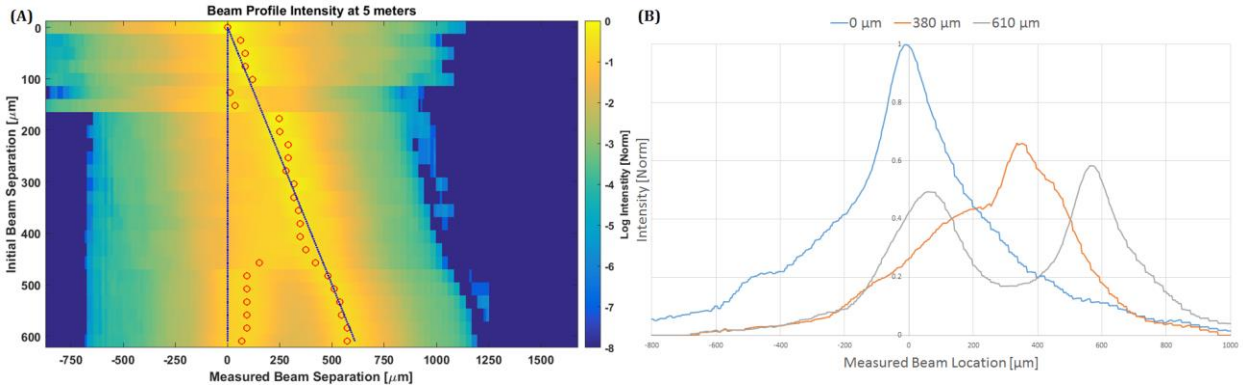

Figure 17 - (a) Surface map of log scale intensities as a function of initial beam separation. (b) Select lineouts to highlight changes in intensity.

Spectral broadening and intensity is enhanced between 480-150 μm of initial beam separation (Figure 18). This indicates an optimal coupling between the beams as when the static beam is located on the border between the dynamic filament's core and reservoir. After ~480 μm of initial beam separation, the beams become distinguishable from each other and UV spectral broadening decreases by ~50 nm. This pattern of spectral broadening can be related to the strength of the cross-Kerr effect and filament competition. At small initial separations (<150 μm), the sub-critical beam is already largely overlapped with the core of the filament. At these separations, the sub-critical beam can interfere and enhance the spectrum of the filament. However, in the range of separations between 480 and 150 μm, the sub-critical beam experiences strong cross-focusing by the filament. The partial overlap of this beam with the reservoir of the filament leads to replenishment of the

filament along propagation, increasing the interaction length for spectral broadening to occur. After 480 μm, the cross-focusing effect on the sub-critical beam is no longer strong enough to attract it into the core of the filament. Instead, the sub-critical beam acts as a seed hot spot for an additional filament, as evidenced by the almost matching peak intensities in Figure 16. The competition between the two filaments over the shared energy in the overlapped photon bath results in a decrease in the spectral broadening and

intensity, There is no spectral data between 730-770 nm due to spectrometer range mismatch.

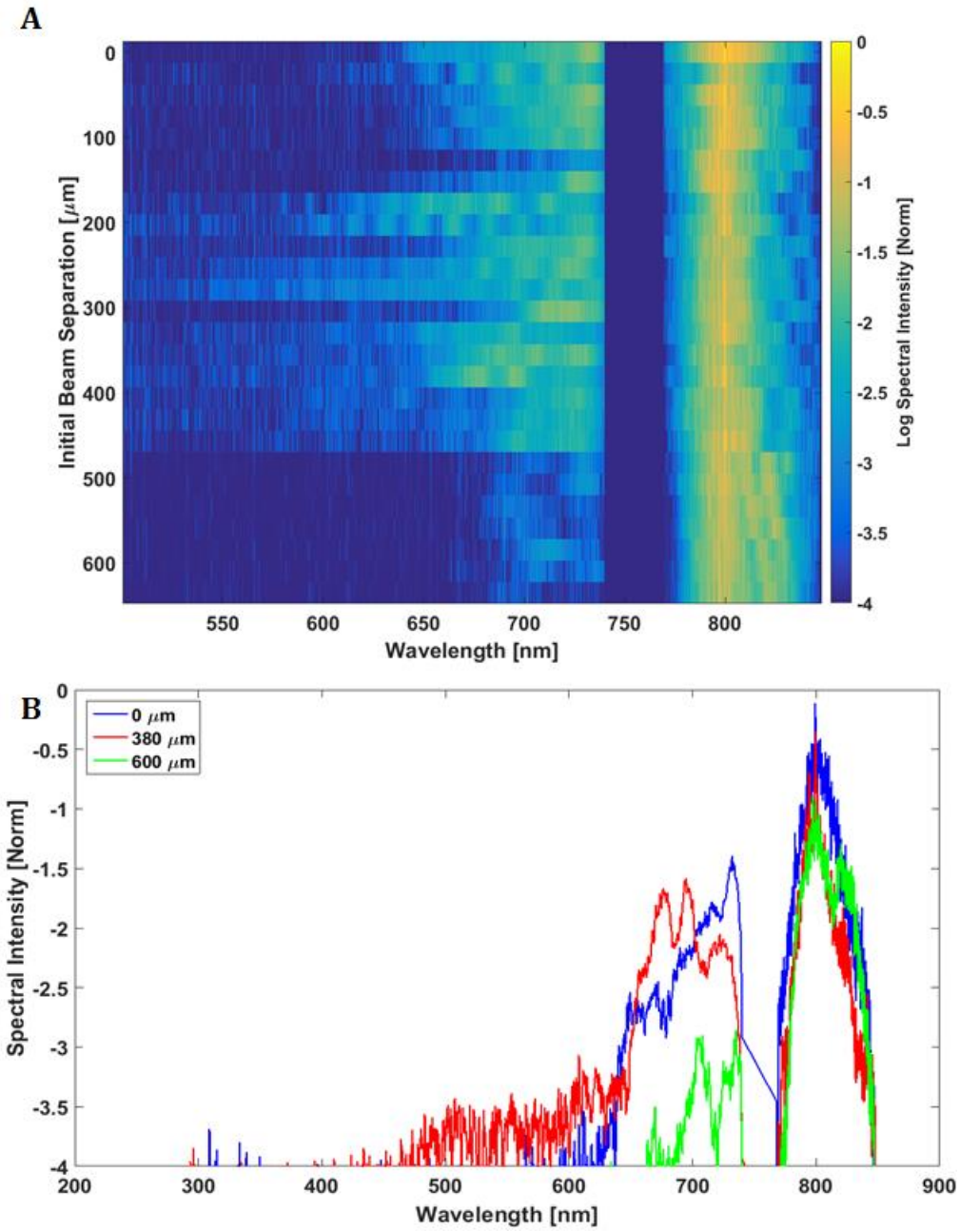

Figure 18 – (a) Combined Spectra of filament and sub-critical beam after 6 meters of propagation from beam combining point. (b) Select spectra at 0 μm (blue), 380 μm (red), and 600 μm (green) initial beam separation compared to spectrum of a noncombined single beam (black).

3.3– Coupling between Two Filaments

Crossing or parallel filaments have been shown to alter numerous features of filamentation [40, 41]. In both cases, by tuning the input parameters of either relative phase or polarization, the amount of XPM experienced by the filaments can be controlled and filament attraction, fusion, repulsion, and energy exchange can be observed. In the experiment performed here the initial energy for both beams is ~1.66 mJ, well above the filamentation threshold (~1.3mJ). Two individual filaments are separated radially from each other to probe the spatial dependence of the coupling between them. The experimental set-up used is similar to the one described in Section 2.2 Figure 6. Both beams are temporally overlapped and have the same polarization. The beam profiles were measured at the geometric focus and the spectra and conical emission profiles were collected one meter beyond the geometric focus.

3.3.1 – Spatial Separation

The beam intensity profiles show attraction between the two filaments (Figure 20). In this case, the energy is closely balanced, though over an average of 500 shots, the dynamic filament (right beam in Figure 20) has ~0.02 mJ more energy.

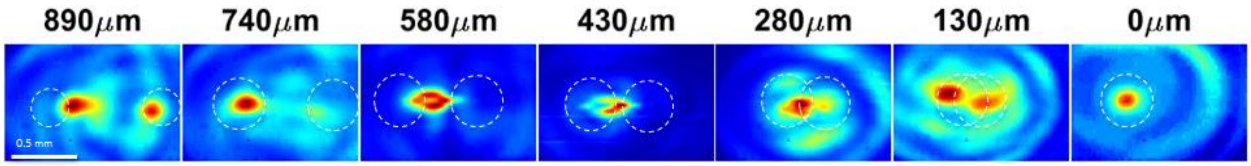

Figure 19 - Beam profiles of two filaments. White circles denote initial separations of the beams.

Unlike Sections 3.1 and 3.2, the beams experience much more balanced mutual attraction to one another. Figure 20 indicates that the beams generally follow the median path between initial separations. Although, below 250 μm initial separation the slightly more energetic dynamic beam still dominates and drags the less energetic static beam. This indicates that when filaments are in close proximity with large regions of filament core overlap (<270 μm initial beam separation), they are more sensitive to energy imbalances that are small when compared to the total energy of the beam. Consistent separation between the filaments doesn't occur until 800 μm of initial beam separation. The peak locations exhibit large instability from one initial beam separation to another, similar to the previous study with sub-critical beams (see Section 3.1). Due to the physical limitations of the size of imaging wedges, larger separations were not possible to measure without substantial clipping.

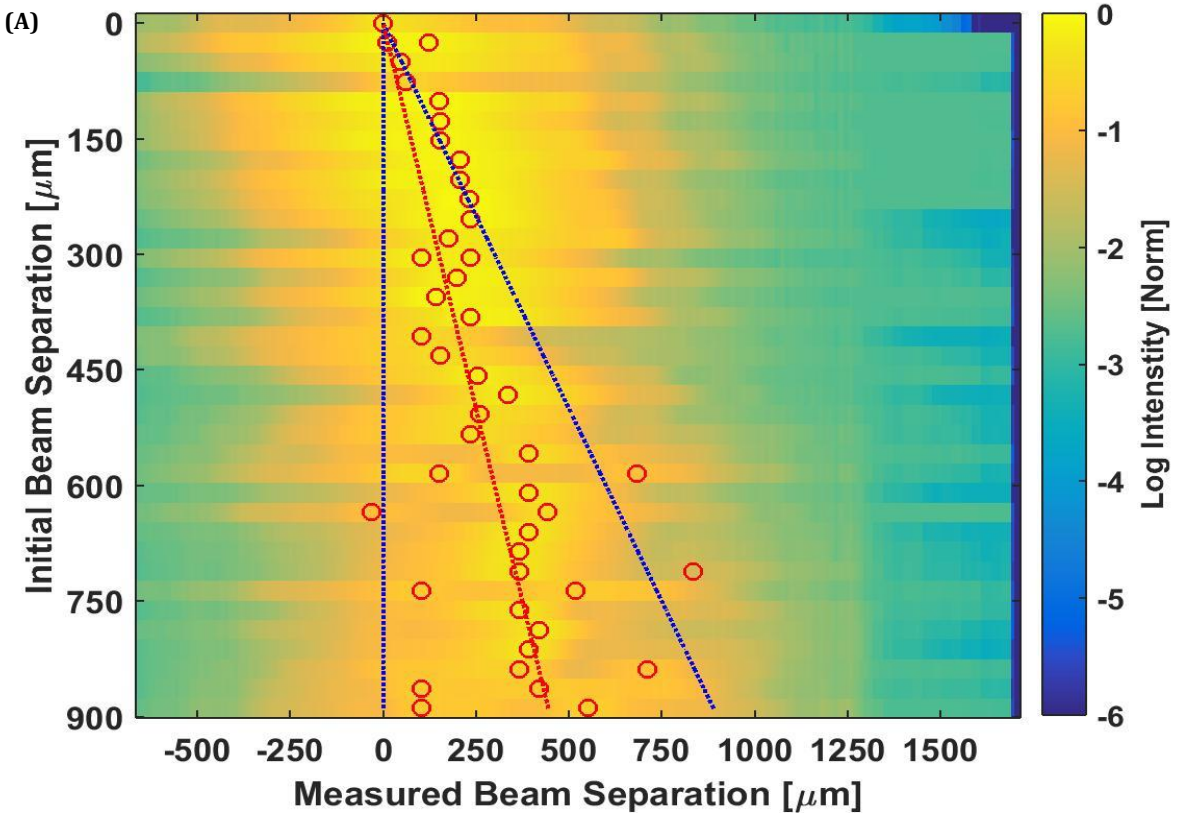

Figure 20 – Beam intensity profiles of two parallel filaments after 5 meters of propagation. Red circles denote peak intensities. Blue lines denote beam locations w/o attraction between the beams. Red line is the mean of the two blue lines.

The combined beam seems to exhibit a tendency to split into multiple filaments orientated orthogonally to the direction of the beam separation (Fig 20, at 580 and 430 μm separation). The frequency of this filament reorientation event occurs approximately between 1:20 and 1:30 shots, depending on the initial beam separation. When there is near complete spatial overlap (<100 μm initial beam separation) the banded filament structure is the dominant structure. This ratio is much lower than the shot-to-shot energy variation in the beam, implying that the structure is likely due to noise from uncontrolled phase or beam pointing variations.

Figure 21 shows spectral broadening in all cases with a significant trend into the UV region, correlating to initial beam separation. The first trend observed is a steady increase in UV broadening up to 200 μm initial separation, decreasing thereafter. This matches up with the regime where the dynamic beam is dominating and strongly attracts the static beam. The overall trend of spectral broadening in the UV shows a distinct dependence on initial beam separation. This effect is the opposite of the spectral broadening seen in Section 3.2, where broadening was enhanced when the sub-critical beam was located on the border of the filament. Here, there exists a local minimum when the two filament cores are either completely overlapped, directly adjacent to each other, or separated far from one another (0, 400, and 900 μm initial beam separation, respectively) and enhanced broadening when the cores are overlapped or exist in each other's reservoir (380-50 and 850-500 μm initial beam separation, respectively). This illustrates the spatial dependence between filament cooperation and filament competition [73].

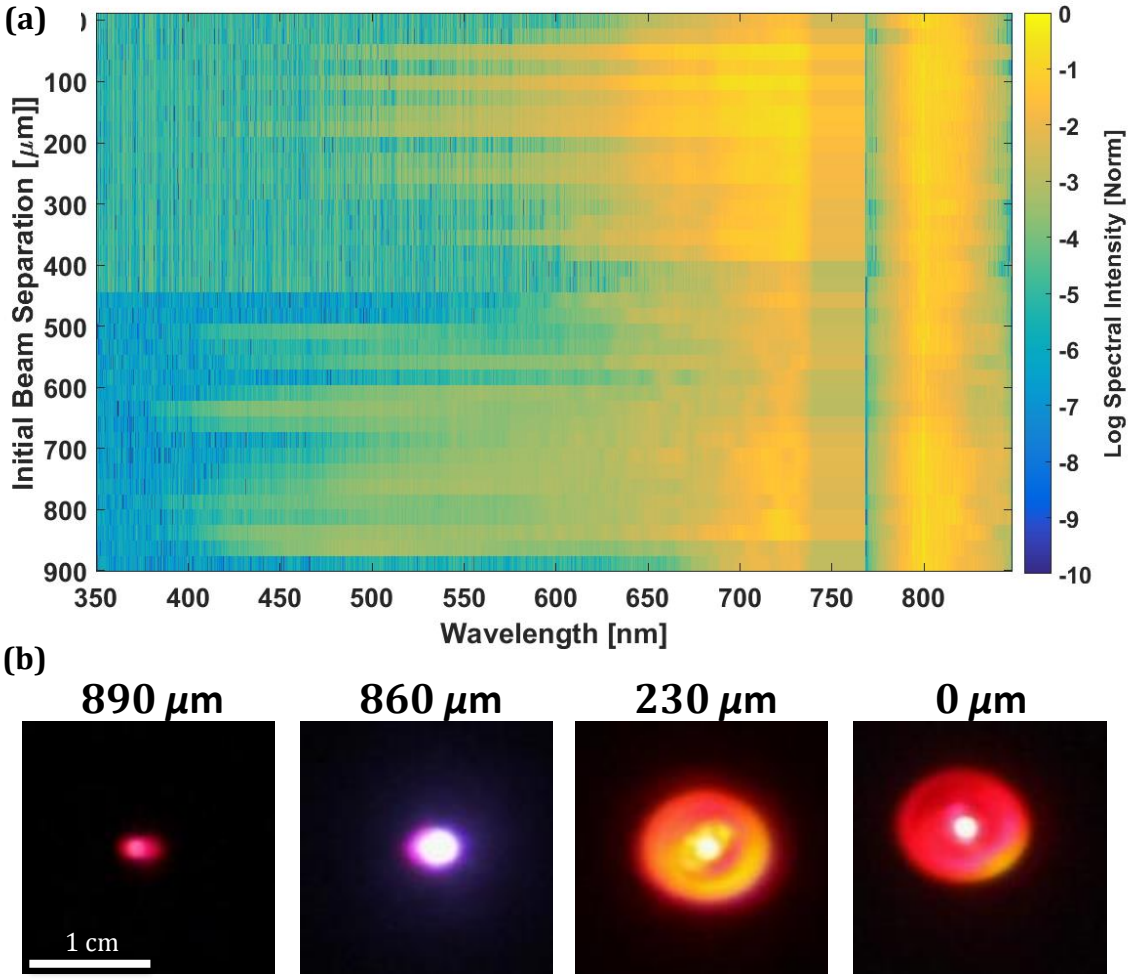

Figure 21 – (a) Spectra and (b) conical emission profiles of combined filaments measured after 6 meters of propagation from point of beam combining.

CHAPTER 4 – CONCLUSION

The dependence of two beams coupling on several input parameters has been investigated. The observations have helped to understand the underlying physics of the spatio-temporal relationships between the two interacting beams.

For many of the potential applications of filaments, arrays of filaments must be engineered to optimally guide waves for long distances in air. The results of this thesis would primarily apply to arrays of such nonlinear beams and would be helpful to create more energy efficient waveguides.

In the first set of experiments, beams well below the threshold for filamentation were shown to exhibit attraction and fusion through the cross-Kerr effect. At large separations, there is coupling of the energy of the reservoir. With sufficient amounts of overlap, two sub-critical beams can generate a filament. The simulations performed indicate that coherently combined beams of sufficient nonlinearity generate broader supercontinnuum more efficiently than a single pulse of equivalent energy.

The second set of experiments confirms the ability of lower intensity beams to pump and enhance filaments in flight and clearly demonstrates the optimal initial positions for such beam-filament pairs.

The experiments with two filaments indicate extremely delicate and sensitive dependences on their interactions, particularly in cases where the initial beam separation cause the two filament core regions to overlap. Stability increases as the cores of the filaments overlap. Spectra exhibit a form of filament cooperation/competition based on beam overlap. When directly adjacent to one another, each filament attempts to replenish itself from the shared peripheral field, resulting in significantly reduced spectral broadening.

The results of the experiments presented in this thesis testify to the intricate nature of nonlinear beam combining and filamentation. The fundamentals of filamentation as a balance of Kerr self-focusing and plasma defocusing have been thoroughly investigated. However, the filamentation process is complex and this complexity compounds itself when considering multiple interacting beams. While many of the results, such as the mutual attraction between two beams, are intuitive, other results, like the irregular spectral broadening of orthogonally polarized beams, leave open questions on the nature of filamentation dynamics. In order to further studies of nonlinear beam combining, improvements to the model must be made. Regardless, the observations made in this thesis will serve as an incremental step towards the understanding of filamentation phenomenon, as well as the applications thereof.

REFERENCES

[1] W. Liu and S. L. Chin, “Direct measurement of the critical power of femtosecond Ti:sapphire laser pulse in air,” *Opt. Express,* vol. 13, no. 15, p. 5750, 2005.

[2] R. Chiao, E. Garmire and C. Townes, “Self-Trapping of Optical Beams,” *Phys. Rev. Lett.,* vol. 13, no. 15, pp. 479-482, 1964.

[3] E. Garmire, R. Chiao and C. Townes, “Dynamics and Characteristics of the Self-Trapping of Intense Light Beams,” *Phys. Rev. Lett.,* vol. 16, no. 9, pp. 347-349, 1966.

[4] A. Braun, G. Korn, X. Liu and e. al., “Self-channeling of high-peak-power femtosecond laser pulses in air,” *Opt. Lett.,* vol. 20, no. 1, p. 73, 1995.

[5] J. Kasparian, P. Rohwetter, L. Woste and J.-P. Wolfe, “Laser-assisted water condensation in the atmosphere: a step towards modulating precipitation?,” *J. Phys. D: Appl. Phys.,* vol. 45, no. 29, p. 293001, 2012.

[6] J. Liu and e. al., “Broadband terahertz wave remote sensing using coherent manipulation of fluorescence from asymmetrically ionized gases,” *Nat. Photonics,* vol. 4, pp. 627-631, 2010.

[7] H. L. Xu and S. L. Chin, “Femtosecond Laser Filamentation for Atmospheric Sensing,” *Sensors,* vol. 11, no. 1, pp. 32-53, 2011.

[8] P. N. Malevich, R. Maurer, D. Kartashov, S. Ališauskas, A. A. Lanin, A. M. Zheltikov, M. Marangoni, G. Cerullo, A. Baltuška and A. Pugžlys, "Stimulated Raman gas sensing by backward UV lasing from a femtosecond filament," *Optics Letters,* vol. 40, no. 11, pp. 2469-2472, 2015.

[9] K. Stelmaszczyk and e. al., “Long-distance remote laser-induced breakdown spectroscopy using filamentation in air,” *Appl. Phys. Lett.,* vol. 85, pp. 3977-3979, 2004.

[10] H. L. Xu, P. T. Simard, J. -F. Daigle, C. Marceau, J. Bernhardt, J. Dubois, M. Châteauneuf, F. Théberge, G. Roy and S. L. Chin, "FilamentInduced Breakdown Remote Spectroscopy in a Polar Environment," *Laser Spectroscopy,* vol. 22, no. 12, pp. 1767-1770, 2012.

[11] S. S. Harilal, J. Yeak and M. C. Phillips, "Plasma temperature clamping in filamentation laser induced breakdown spectroscopy," *Optics Express,* vol. 23, no. 21, pp. 27113-27122, 2015.

[12] N. Jhajj and e. al., “Demonstration of Long-Lived High-Power Optical Waveguides in Air,” *Phys. Rev. X,* vol. 4, p. 011027, 2014.

[13] O. Lahav and e. al., “Long-lived waveguides and sound-wave generation by laser filamentation,” *Phys. Rev. A,* vol. 90, p. 021801(R), 2014.

[14] Z. A. Kudyshev, M. C. Richardson and N. M. Litchinitser, “Virtual hyperbolic metamaterials for manipulating radar signals in air,” *Nat. Comm.,* vol. 4, p. 2557, 2013.

[15] Y. Ren and M. Alshershby, “Microwave guiding in air along single femtosecond laser filament,” *J. Appl. Phys.,* vol. 113, pp. 094904-5, 2013.

[16] M. Alshershby and e. al., “Guiding microwave radiation using laser-induced filaments: the hollow conducting waveguide concept,” *J. Phys. D: Appl. Phys.,* vol. 45, p. 265401, 2012.

[17] A. Camino and e. al., “Femtosecond filament array generated in air,” *Appl. Phys. B,* vol. 121, pp. 363-368, 2015.

[18] M. Mlejnek, M. Kolesik, J. V. Moloney and E. M. Wright, "Optically Turbulent Femtosecond Light Guide in Air," *Phys. Rev. Lett. ,* vol. 83, p. 2938, 1999.

[19] D. V. Apeksimov and e. al., "Control of the domain of multiple filamentation of terawatt laser pulses along a hundred-meter air path," *Quantum Elec.,* vol. 45, no. 5, p. 408, 2015.

[20] Y. Fu and e. al., "Control of filament branching in air by astigmatically focused femtosecond laser pulses," *Appl. Phys. B,* vol. 103, no. 2, pp. 435-439, 2011.

[21] T. D. Grow and A. L. Gaeta, "Dependence of multiple filamentation on beam ellipticity," *Opt. Express,* vol. 13, pp. 4594-4599, 2005.

[22] N. Barbieri and e. al., "Double helical laser beams based on interfering first-order Bessel beams," *J. Opt. Soc. Am. A,* vol. 28, pp. 1462-1469, 2011.

[23] A. Couairon and A. Mysyrowicz, "Femtosecond filamentation in transparent media," *Phys.Rep.,* vol. 441, no. 2-4, pp. 47-189, 2007.

[24] S. L. Chin and e. al., "Advances in intense femtosecond laser filamentation in air," *Laser Phys.,* vol. 22, no. 1, pp. 1-53, 2011.

[25] E. T. Nibbering, "Determination of the inertial contribution to the nonlinear refractive index of air, N2, and O2 by use of unfocused high-intensity femtosecond laser pulses," *J. Opt. Soc. Am. B,* vol. 14, pp. 650-660, 1997.

[26] R. Coso and J. Solis, "Relation between nonlinear refractive index and third-order susceptibility in absorbing media," *J. Opt. Soc. Am.,* vol. 21, no. 3, pp. 640-644, 2004.

[27] R. W. Boyd, Nonlinear Optics, Boston, Mass.: Academic, 1992.

[28] P. Kelley, "Self-Focusing of Optical Beams," *Phys. Rev. Lett.,* vol. 15, no. 26, pp. 1005-1008, 1965.

[29] J. H. Marburger, "Self-focusing: theory," *Progr. Quantum Electron,* vol. 4, pp. 35-110, 1975.

[30] J.-C. Diels and W. Rudolph, Ultrashort Laser Pulse Phenomena, 2nd ed., Academic Press, 2006, p. 680.

[31] A. Couairon, G. Mechain and e. al., "Infrared femtosecond light filaments in air: simulations and experiments," *J. Opt. Soc. Am. B,* vol. 19, no. 5, p. 1117, 2002.

[32] M. Kolesik and e. al., "Physical factors limiting the spectral extent and band gap dependence of supercontinuum generation," *Phys. Rev. Lett.,* vol. 91, p. 043905, 2003.

[33] M. Durand, *Filamentation laser femtoseconde IR : Interaction de deux filaments et Source de rayonnement secondaire longue distance,* Palaiseau: Ecole Polytechnique X, 2011.

[34] C. D'Amico and e. al., "Forward THz radiation emission by femtosecond filamentation in gases: theory and experiment," *New J. Phys.,* vol. 10, no. 1, p. 013015, 2008.

[35] M. Mlejnek and e. al., "Dynamic spatial replenishment of femtosecond pulses propagating in air," *Opt. Lett.,* vol. 23, no. 5, p. 382, 1998.

[36] E. McKee, *FEMTOSECOND FILAMENT INTERACTION AS A PROBE FOR MOLECULAR ALIGNMENT,* Orlando: University of Central Florida, 2012.

[37] W. Liu and e. al., "Experiment and simulations on the energy reservoir effect in femtosecond light filaments," *Opt. Lett.,* vol. 30, pp. 2602-2604, 2005.

[38] R. Bernath, *High-Intensity Ultra-Fast Laser Interaction Technologies,* Orlando: University of Central Florida, 2007.

[39] C. Jeon, D. Harper, K. Lim, M. Durand, M. Baudelet and M. C. Richardson, "Interaction of a single laser filament with a single aerosol," *J. of Optics,* vol. 17, p. 055502, 2015.

[40] B. Shim and e. al., "Controlled interactions of femtosecond light filaments in air," *Phys. Rev.,* vol. 81, p. 061803(R), 2010.

[41] J. Wu and e. al., "Interaction of two parallel femtosecond filaments at different wavelengths in air," *Opt. Lett.,* vol. 34, pp. 3211-3213, 2009.

[42] J. Liu and e. al., "Two-dimensional plasma grating by non-collinear femtosecond filament interaction in air," *Appl. Phys.,* vol. 99, p. 151105, 2011.

[43] Y. Ren, M. Alshershby, Z. Hao, Z. Zhao and J. Lin, "Microwave guiding along double femtosecond filaments in air," *Phys. Rev. E,* vol. 88, p. 013104, 2013.

[44] H. Gao, W. Chu, G. Yu, B. Zeng, J. Zhao, Z. Wang, W. Liu, Y. Cheng and Z. Xu, "Femtosecond laser filament array generated with step phase plate in air," *Optics Express,* vol. 21, no. 4, pp. 4612-4622, 2013.

[45] W. Walasik and M. Litchinitser, *Dynamics of large femtosecond filament arrays: possibilities, limitations, and trade-offs,* 2015.

[46] H. Pepin and e. al., "Triggering and guiding high-voltage large-scale leader discharges with sub-joule ultrashort laser pulses," *Physics of Plasma,* vol. 8, pp. 2532-2539, 2001.

[47] M. Rodriguez, R. Sauerbrey, H. Wille, L. Wöste, T. Fujii, Y. -B. André, A. Mysyrowicz, L. Klingbeil, K. Rethmeier, W. Kalkner, J. Kasparian, E. Salmon, J. Yu and J. -P. Wolf,

"Triggering and guiding megavolt discharges by use of laser-induced ionized filaments," *Optics Letters,* vol. 27, no. 9, pp. 772-774, 2002.

[48] B. La Fontaine and e. al., "Guiding large-scale spark discharges with ultrashort pulse laser filaments," *J. Appl. Phys.,* vol. 88, p. 610, 2000.

[49] S. B. Leonov, A. A. Firsov, M. A. Shurupov, J. B. Michael, M. N. Shneider, R. B. Miles and N. A. Popov, "Femtosecond laser guiding of a high-voltage discharge and the restoration of dielectric strength in air and nitrogen," *Physics of Plasmas,* vol. 19, p. 123502, 2012.

[50] J. Kasparian, R. Sauerbrey and S. L. Chin, "The critical laser intensity of self-guided light filaments in air," *Appl. Phys. B,* vol. 71, p. 877, 2000.

[51] P. Bejot, J. Kasparian, S. Henin, V. Loriot, T. Vieillard, E. Hertz, O. Faucher, B. Lavorel and J. -P. Wolf, "Higher-order Kerr terms allow ionization-free filamentation in gases," *Phys. Rev. Lett.,* vol. 104, p. 103903, 2010.

[52] M. Kolesik, E. M. Wright and J. V. Moloney, "Femtosecond filamentation in air and higher-order nonlinearities," *Opt. Lett.,* vol. 35, p. 2550, 2010.

[53] C. Bree, A. Demircan and G. Steinmeyer, "Saturation of the all-optical Kerr effect," *Phys. Rev. Lett.,* vol. 106, p. 183902, 2011.

[54] C. Kohler, R. Guichard, E. Lorin, S. Chelkowski, A. D. Bandrauk, L. Berge and S. Skupin, "Saturation of the nonlinear refractive index in atomic gases," *Phys. Rev. A,* vol. 87, p. 043811, 2013.

[55] P. Bejot, E. Cormier, E. Hertz, B. Lavorel, J. Kasparian and J. -P. Wolf, "High-field quantum calculation reveals time-dependent negative Kerr contribution," *Phys. Rev. Lett.,* vol. 110, p. 043902, 2013.

[56] J. K. Wahlstrand and H. M. Milchberg, "Effect of a plasma grating on pump-probe experiments near the ionization threshold in gases," *Opt. Lett.,* vol. 36, p. 3822, 2011.

[57] G. Fibich and B. Ilan, "Self-focusing of circularly polarized beams," *Phys. Rev. E,* vol. 67, p. 036622, 2003.

[58] N. A. Panov and e. al., "Filamentation of femtosecond Gaussian pulses with close-to-linear or -circular elliptical polarisation," *Quantum Electronics,* vol. 41, pp. 160-162, 2011.

[59] M. Ammosov, S. Lazaresku, S. Augst and e. al., "Polarization Effect during Strong-Field Ionization of Atoms," *Laser Phys.,* vol. 7, no. 3, pp. 706-708, 1997.

[60] M. Kolesik, J. V. Moloney and E. M. Wright, "Polarization dynamics of femtosecond pulses propagating in air," *Phys. Rev. E,* vol. 64, no. 4, p. 046607, 2001.

[61] A. Srivastava and D. Goswami, "Polarization-induced modulation of a femtosecond nonlinear process," *Phys. Lett. A,* vol. 341, no. 5-6, pp. 523-526, 2005.

[62] A. S. Sandhu, S. Banerjee and D. Goswami, "Suppression of supercontinuum generation with circularly polarized light," *Op. Commun.,* vol. 181, no. 1-3, pp. 101-107, 2000.

[63] J. Liu, X. W. Chen, R. X. Li and e. al., "Polarization-dependent pulse compression in an argon-filled cell through filamentation," *Laser Phys. Lett.,* vol. 5, no. 1, pp. 45-47, 2008.

[64] H. Yang, J. Zhang, Q. Zhang and e. al., "Polarization-dependent supercontinuum generation from light filaments in air," *Opt. Lett.,* vol. 30, no. 5, p. 534, 2005.

[65] K. Lim, *Laser Filamentation - Beyond Self-focusing and Plasma Defocusing,* Orlando: University of Central Florida, 2014.

[66] H. Cai, J. Wu, H. Li, X. Bai and H. Zeng, "Elongation of femtosecond filament by molecular alignment in air," *Opt. Express,* vol. 17, no. 23, p. 21060, 2009.

[67] J. Wu, H. Cai, A. Couairon and H. Zeng, "Wavelength tuning of a few-cycle laser pulse by molecular alignment," *Phys. Rev. A,* vol. 79, no. 6, p. 063812, 2009.

[68] P. Béjot, Y. Petit, L. Bonacina, J. Kasparian, M. Moret and J.-P. Wolf, "Ultrafast gaseous "half-wave plate"," *Opt. Express,* vol. 16, no. 10, p. 7564, 2008.

[69] O. Kosareva, N. Panov, V. Makarov, I. Perezhogin, C. Marceau, Y. Chen, S. Yuan, T. Wang, H. Zeng, A. Savel'ev and S. L. Chin, "Polarization rotation due to femtosecond filamentation in an atomic gas," *Opt. Lett.,* vol. 35, no. 17, pp. 2904-2906, 2010.

[70] S. Yuan, T.-J. Wang, O. Kosareva, N. Panov, V. Makarov, H. Zeng and S. L. Chin, "Measurement of birefringence inside a filament," *Phys. Rev. A,* vol. 84, p. 013838, 2011.

[71] D. Faccio, A. Averchi, A. Couairon, M. Kolesik, J. Moloney, A. Dubietis, G. Tamosauskas, P. Polesana, A. Piskarskas and P. Di Trapani, "Spatio-temporal reshaping and X Wave dynamics in optical filaments.," *Opt. Express,* vol. 15, pp. 13077-13095, 2007.

[72] L. Berge and e. al., "Multiple Filamentation of Terawatt Laser Pulses in Air," *Phys. Rev. Lett.,* vol. 92, no. 22, p. 225002, 2004.

[73] S. A. Hosseini and e. al., “Competition of multiple filaments during the propagation of intense femtosecond laser pulses,” *Phys. Rev. A,* vol. 70, p. 033802, 2004.

[74] S. L. Chin, S. Petit, W. Liu, A. Iwasaki, M. -C. Nadeau, V. P. Kandidov, O. G. Kosareva and K. Y. Andrianov, "Interference of transverse rings in multifilamentation of powerful femtosecond laser pulses in air," *Opts. Commun.,* vol. 210, pp. 329-341, 2002.

[75] Q. Lou, S. A. Hosseini, J. -F. Gravel, O. G. Kosarvera, N. A. Panov, N. Akozbek, V. P. Kandidov, G. Roy and S. L. Chin, "Effect of beam diameter on the propagation of intense femtosecond laser pulses," *Appl. Phys. B,* vol. 80, pp. 35-38, 2005.

[76] Q. Luo and e. al., “Effect of beam diameter on the propagation of intense femtosecond laser pulses,” *Appl. Phys. Lett. B-Lasers and Optics,* vol. 80, pp. 35-38, 2005.

[77] G. Fibich, S. Eisenmann, B. Ilan and A. Zigler, “Control of multiple filamentation in air,” *Opt. Lett.,* vol. 29, pp. 1772-1774, 2004.

[78] N. Barbieri, *Engineering and Application of Ultrafast Laser Pulses and Filamentation in Air,* University of Central Florida, 2013.

[79] L. Liu and e. al., “Fine control of multiple femtosecond filamentation using a combination of phase plates,” *J. Phys. B: Atomic, Molecular and Optical Physics,* vol. 44, p. 215404, 2011.

[80] N. Barbieri and e. al, “Helical Filaments,” *Appl. Phys. Lett.,* vol. 104, no. 26, p. 261109, 2014.

[81] E. B. Treacy, “Chirped Optical Pulses,” *IEEE J Quant. Elect.,* vol. 5, p. 454, 1969.

[82] M. Mlejnek, E. M. Wright and J. V. Moloney, “Moving-focus versus self-waveguiding model for long-distance propagation of femtosecond pulses in air,” *IEEE J. Quantum Electron.,* vol. 35, no. 12, pp. 1771-1776, 1999.

[83] J. -F. Ripoche, G. Grillon, P. B., M. Franco, E. Nibbering, R. Lange and A. Mysyrowicz, "Determination of the time dependence of ~1, in air," *Opt. Commun.,* vol. 135, pp. 310-314, 1997.

[84] S. R. Deans, The Radon Transform and Some of Its Applications, New York: Wiley, 1983.

[85] H. Cai, J. Wu, P. Lu, X. Bai, L. Ding and H. Zeng, "Attraction and repulsion of parallel femtosecond filaments in air," *Physical Review A,* vol. 80, p. 051802(R), 2009.

[86] A. Trisorio and C. P. Hauri, “Control and characterization of multiple circularly polarized femtosecond filaments in argon,” *Opt. Lett. ,* vol. 32, pp. 1650-1652, 2007.

[87] S. L. Chin and e. al., “Interference of transverse rings in multifilamentation of powerful femtosecond laser pulses in air,” *Opt. Commun.,* vol. 210, pp. 329-341, 2002.

[88] K. Lim, M. Durand, M. Baudelet and M. Richardson, “Transition from linear- to nonlinear-focusing regime in filamentation,” *Scientific Reports,* vol. 4, p. 7217, 2014.

[89] Y. Chen and e. al., “Observation of filamentation-induced continuous self-frequency down shift in air,” *Appl. Phys.B,* vol. 91, pp. 219-222, 2008.

[90] F. Theberge and e. al., “Generation of tunable and broadband far-infrared laser pulses during two-color filamentation,” *Phys. Rev. A,* vol. 81, p. 033821, 2010.

[91] M. S. Mills, M. Heinrich, M. Kolesik and D. Chistodoulides, “Extending optical filaments using auxiliary dress beams,” *J. Phys. B: Atomic, Molecular and Optical Physics,* vol. 48, no. 9, p. 094014, 2015.

[92] S. Petit, A. Talebpour, A. Proulx and S. Chin, “Polarization dependence of the propagation of intense laser pulses in air,” *Opt. Commun.,* vol. 175, p. 323, 2000.

[93] G. P. Agrawal, Nonlinear Fiber Optics, 5th ed., New York: Academic Press, 2013.

[94] P. Béjot, Y. Petit, L. Bonacina, J. Kasparian, M. Moret and J. -P. Wolf, "Ultrafast gaseous “half-wave plate”," *Optics Express,* vol. 16, no. 10, pp. 7564-75707, 2008.

[95] E. W. Weisstein, "http://mathworld.wolfram.com/Circle-CircleIntersection.html," MathWorld. [Online]. [Accessed March 2016].